University of Groningen

Pionic fusion in light-ion systems

Joulaeizadeh, Leila

IMPORTANT NOTE: You are advised to consult the publisher's version (publisher's PDF) if you wish to cite from it. Please check the document version below.

Document Version
Publisher's PDF, also known as Version of record

Publication date:
2009

Link to publication in University of Groningen/UMCG research database

Citation for published version (APA):
Joulaeizadeh, L. (2009). *Pionic fusion in light-ion systems*. [Thesis fully internal (DIV), University of Groningen]. s.n.

Copyright
Other than for strictly personal use, it is not permitted to download or to forward/distribute the text or part of it without the consent of the author(s) and/or copyright holder(s), unless the work is under an open content license (like Creative Commons).

The publication may also be distributed here under the terms of Article 25fa of the Dutch Copyright Act, indicated by the "Taverne" license. More information can be found on the University of Groningen website: https://www.rug.nl/library/open-access/self-archiving-pure/taverne-amendment.

Take-down policy
If you believe that this document breaches copyright please contact us providing details, and we will remove access to the work immediately and investigate your claim.

Downloaded from the University of Groningen/UMCG research database (Pure): http://www.rug.nl/research/portal. For technical reasons the number of authors shown on this cover page is limited to 10 maximum.

Download date: 05-05-2023

5. Analysis of the ^{6}Li(^{4}He,π^0)^{10}B* data

5.1 Introduction

In this chapter, we discuss the analysis of the ^{6}Li(^{4}He,π^0)^{10}B* reaction at T_{beam}=236.4 MeV. The basic steps of the analysis procedure are schematically illustrated in Fig. 5.1. Each of the elements in Fig. 5.1 is discussed separately.

In the first part, referred to in the figure as "Identification", different techniques and available information are used to identify photons in the Plastic Ball and the Inner Shell part of the setup as well as ions in the Heavy Ion detector which is positioned in the focal plane of the Big-Bite Spectrometer. The method of identification is explained in Section 5.2. The "Calibration" part, which is followed in Section 5.3, involves the calibration of the time information of the Plastic Ball, the Inner Shell and the Heavy Ion detectors. In addition, the energy calibration of the Plastic Ball and the Inner Shell, and the gain matching of the Heavy Ion detector modules as well as the momentum calibration of the Heavy Ion detector array are included in this section. The following Section 5.4 discusses the selection of the ^{6}Li(^{4}He,π^0)^{10}B* events. This includes the presorting of the data ("Presort"), the reconstruction of the ^{6}Li(^{4}He,π^0)^{10}B* kinematics ("Event reconstruction") and

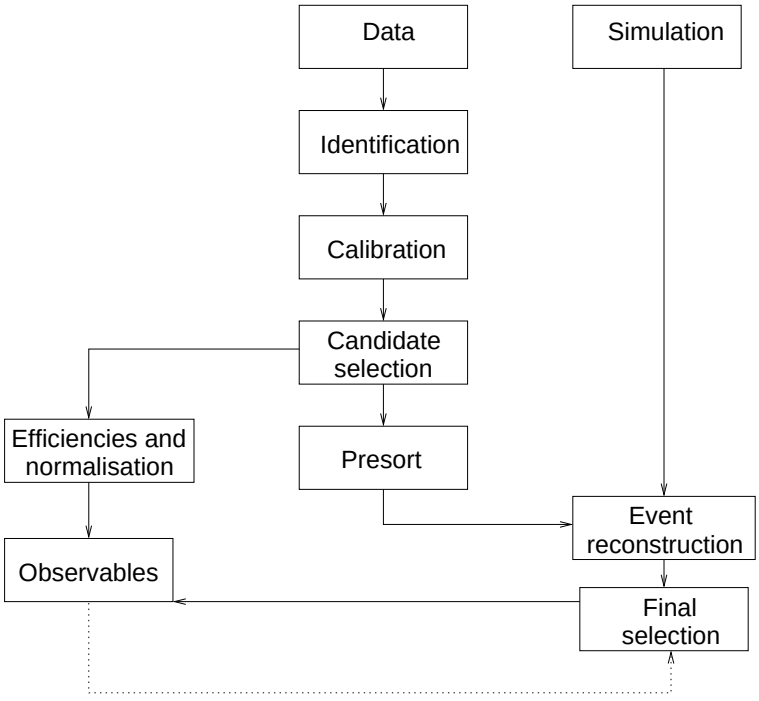

Figure 5.1: A schematic representation of the analysis method used to obtain ^{6}Li(^{4}He,π^0)^{10}B* events and the corresponding observables. For a complete description see the text.

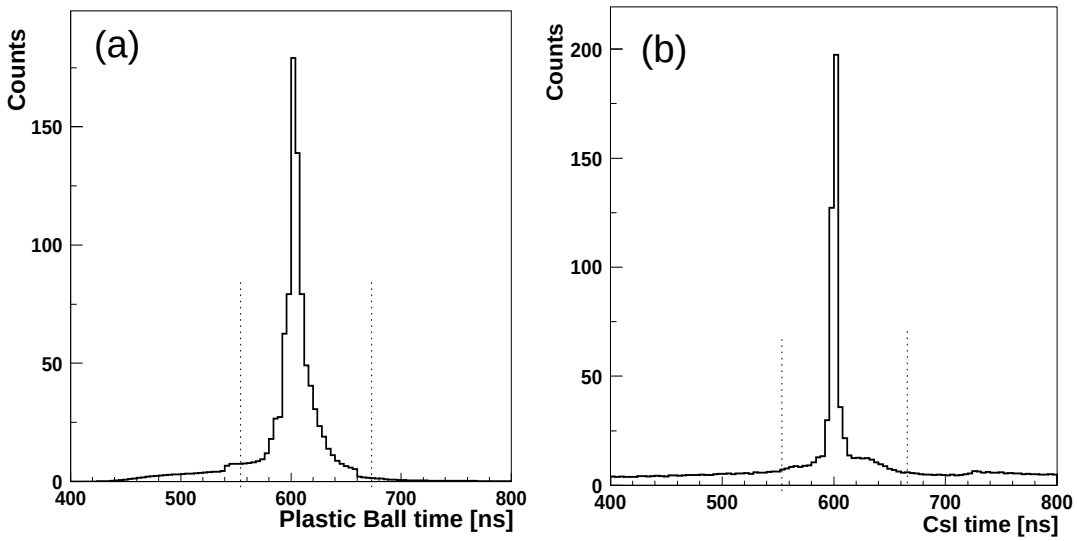

Figure 5.2: The timing information of the Plastic Ball and the Inner Shell detectors summed over all modules. Events under the sharp peaks (between the two vertical dashed-lines) are associated with the same time difference between the signal after the Ball Boxes and the Plastic Ball-single or the Inner Shell-single triggers for all modules. Events outside of the peaks are due to the random coincidences and are excluded from the analysis.

the final selection to obtain background-free ^{6}Li(^{4}He,π^{0})^{10}B* events ("Final selection"). Furthermore, it is explained how the Plastic Ball modules are grouped to make a cluster of detectors hit by a particle. In Section 5.5, we present the results of the background estimation. In order to obtain absolute values for the cross sections, an accurate determination of detector efficiencies is important. In Sections 5.6 and 5.7 the analysis of this process, which is labelled in Fig. 5.1 as "Efficiencies and normalisation", is described.

5.2 Particle identification

5.2.1 Photon identification

The Plastic Ball and the Inner Shell time

As was explained in Chapter 4, recording of the timing information by the TDCs (Time-to-Digital Converters) of the Plastic Ball and the Inner Shell detectors starts when the individual detector is hit and commonly stops when the single trigger is issued. The time difference between start and stop for one detector module depends on the difference in the wire lengths which are travelled by one or the other signal sent to the TDCs or to the trigger box. Figure 5.2-(a) and (b) shows the recorded time summed over all modules for the Plastic Ball detector and the Inner Shell detector, respectively. For events contained in the sharp peaks ($t = 610 \pm 60$ ns), the signals which start and stop the TDC are correlated in time. Events outside the sharp peaks are associated with random coincidences.

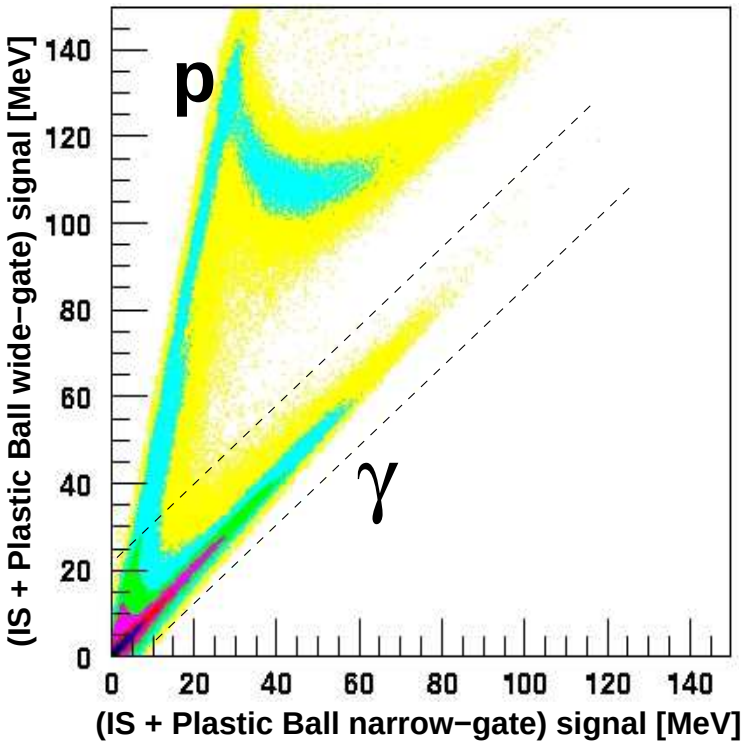

Figure 5.3: The calibrated Plastic Ball plus Inner Shell pulse shape and identification of photons. The spectrum is summed over all modules. Regions labelled "p" and "γ" represent protons and photons, respectively.

The Plastic Ball pulse shape

Figure 5.3 shows the two-dimensional spectrum (pulse shape spectrum) for the particle identification of protons and photons. The vertical axis shows the sum of the Inner Shell, the CaF_2 and the plastic light output using the wide-gate integration of the Plastic Ball and the Inner Shell signals within 944 ns. The horizontal axis shows the sum of the Inner Shell and the plastic signals using the narrow-gate integration with the gates of 944 ns and 133 ns width, respectively. The regions labelled "p" and "γ" represent the associated events with protons and photons, respectively. Photon events are populated around the diagonal line. The events associated with charged particles which are mainly protons, are well separated from the locus of photon events.

5.2.2 Ion identification

A two-dimensional spectrum was produced using the wide- and narrow-gate integration of the signal for a Heavy Ion detector module in coincidence with two photons in the Plastic Ball (Fig. 5.4). The horizontal and the vertical axes represent wide- and narrow-gate integrations, respectively, in one Heavy Ion detector module. Using the QDC modules, the result of the narrow-gate integration has been amplified by a factor of 5. The narrow-gate integration is supposed to represent the light output of the 80 μm thick plastic scintillator,

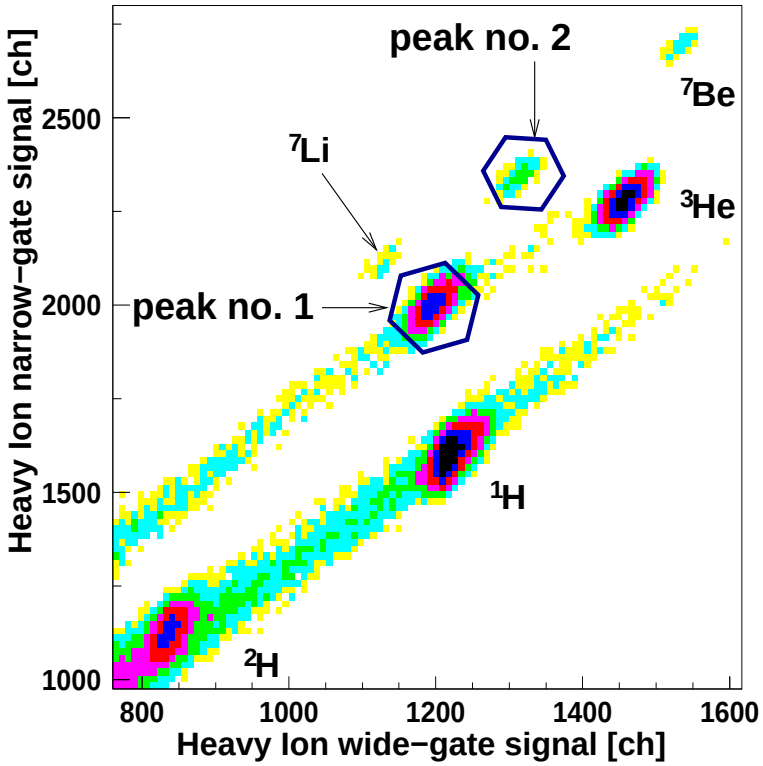

Figure 5.4: The Heavy Ion pulse shape and identification of isotopes. The horizontal and the vertical axes represent wide- and narrow-gate integrations, respectively, in one Heavy Ion detector module.

while the wide-gate integration shows the total light output of the plastic and the CsI(Tl) scintillators. Every peak in the pulse shape spectrum corresponds to one ion species. As can be seen, using the pulse shape techniques each peak is well separated. To identify ions, different tools were employed as explained in the following sections.

Ion Time Of Flight

Using the TDCs of the Heavy Ion detector modules, the time difference between ion and photon detections was recorded. This time difference is proportional to the Time Of Flight (TOF) of ions from the target to the Heavy Ion detector while passing through the Big-Bite Spectrometer. The Time Of Flight is calculated as:

$$TOF = \frac{mL}{qB\rho}, \tag{5.1}$$

with q being the charge, m the particle mass, L the length passed by the ion from the target into the Heavy Ion detector (typ. 7.5 m), B the magnetic field and ρ the radius of the trajectory in the dipole magnetic field. As can be seen in Fig. 5.5-(a), using Time Of Flight information most of the produced ions have been identified. ^{10}B ions, produced in the pionic fusion reaction, as well as ^{6}Li and ^{4}He, produced in the elastic interaction

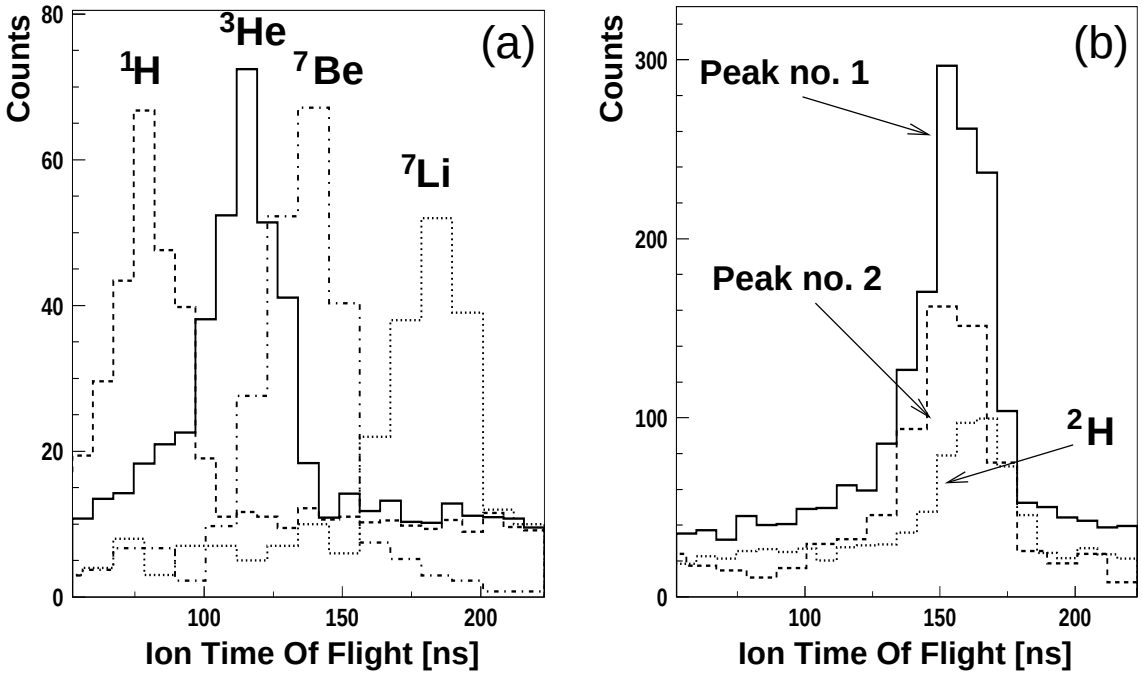

Figure 5.5: Calibrated Time Of Flight of ions from the target to the Heavy Ion detector by passing through the Big-Bite Spectrometer. The original recorded time is the time difference between the ion and the photon detection which is proportional to the Time Of Flight of the ion from the target to the Heavy Ion detector. Using the kinematical calculations and the magnetic field of the Big-Bite Spectrometer, the original recorded time difference is converted into the Time Of Flight.

of ^{4}He with ^{6}Li, and ^{2}H have the same m/q ratio (Fig. 5.5-(b)). Therefore, the Time Of Flight information is not sufficient to identify the peak for the ^{10}B events among the peaks in Fig. 5.4. In order to obtain a unique identification of ^{10}B, other available information is required.

Ion energy deposition

The momentum acceptance strongly suppresses the elastically scattered ^{4}He and ^{6}Li in the focal plane of the Big-Bite Spectrometer. However, we aimed at a unique identification of the fusion product to suppress background caused by incomplete detection of photons from neutral pion decay. We used all the available information like the light output of the scintillators for different produced particles. Due to the high ionisation of charged particles inside the scintillators, the scintillator response to the energy deposition of the charged particles is not linear. In fact, a fraction of the deposited energy inside the scintillators is not converted into the light output. This effect is called "quenching". Horn et al. [60, 61] have measured the response of plastic and CsI(Tl) scintillators for a variety of nuclear species between ^{1}H and ^{12}C as a function of atomic number, mass number and energy (up to 37 MeV/nucleon for ^{12}C ions) and have studied the strong quenching effects. Figure 5.6 shows the result of their calibration for the CsI(Tl) scintillators. Data-points

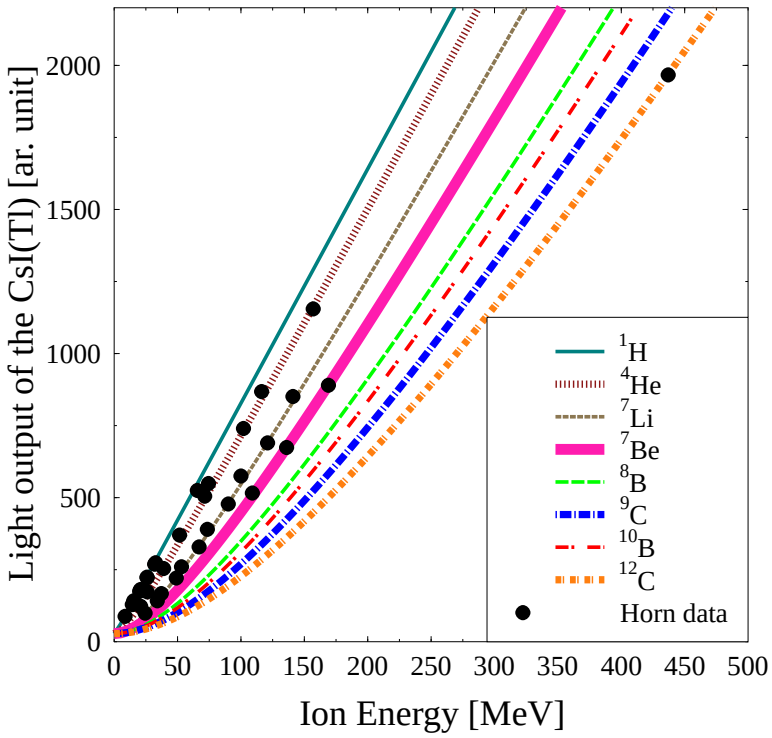

Figure 5.6: Calibration curves for the CsI(Tl) scintillators obtained in the measurement done by Horn et al. [60]. The circles are the data points resulting from their experiment while the curves are the result of a least-squares fit by using Eq.(5.2).

are the experimental results which have been fitted to the light output using the following expression:

$$L = a_0 + a_1(E - a_2AZ^2 ln|\frac{E + a_2AZ^2}{a_2AZ^2}|), \tag{5.2}$$

where a_0, a_1 and a_2 are the electronics offset factor, electronics gain factor and the quenching factor, respectively. E, A and Z are the ion energy, the ion mass and the ion charge, respectively. Calibration factors from Horn's experiment were used as a tool to identify different ions in the Heavy Ion detector. We compared the relative light output of the Heavy Ion detector for different ions with the relative light output of the Horn measurement.

In case of the Heavy Ion detector, using the narrow-gate integration, mainly the plastic light output is integrated. However, in the narrow-gate integration there is always some contribution of the light output from the CsI(Tl) scintillator. Also the result of the wide-gate integration consists of the total light output of the module which includes the plastic

and the CsI(Tl) light output. Therefore, the first step of the ion identification was to obtain the pure plastic and the pure CsI(Tl) light output of the Heavy Ion detector. For that purpose the results of the Horn calibration of the light output were used to determine the scaling factors of the plastic light output to the total contribution and the CsI(Tl) light output to the total contribution as follows:

$$L_{CsI(Tl)}(HIdet) = L_{total}(HIdet) - \frac{L_{pl}(Horn)}{L_{CsI(Tl)}(Horn) + L_{plastic}(Horn)} \times L_{total}(HIdet), \tag{5.3}$$

$$L_{plastic}(HIdet) = L_{total}(HIdet) - \frac{L_{CsI(Tl)}(Horn)}{L_{CsI(Tl)}(Horn) + L_{plastic}(Horn)} \times L_{total}(HIdet), \tag{5.4}$$

where $L_{CsI(Tl)}(HIdet)$ and $L_{CsI(Tl)}(Horn)$ are the light output of the CsI(Tl) scintillators of the Heavy Ion detector module and the Horn detector, respectively. $L_{plastic}(HIdet)$ and $L_{plastic}(Horn)$ are the light output of the plastic scintillators of the Heavy Ion detector module and the Horn detector, respectively. $L_{total}(HIdet)$ indicates the total light output of the Heavy Ion detector module using the wide-gate integration.

The detector light output as a function of particle charge for the Horn measurement and the present measurement is depicted in Fig. 5.7 left and right panels, respectively. The error bars in Fig. 5.7-(b) and -(d) are the standard deviations of the peaks in the pulse shape spectrum of the Heavy Ion detector (Fig. 5.4). The error bars in Fig. 5.7-(c) originate from the uncertainty in the determination of a_0, a_1 and a_2 in Eq. 5.2. Fig. 5.7-(a) and -(b) shows the pure light output of the plastic scintillator from our data (b) and from the Horn data (a) for particles which hit the Heavy Ion detector. The full circle and full square in the Fig. 5.7-(b) are the results for the "peak number 1" and "peak number 2" in the pulse shape spectrum of the Heavy Ion detector, when assuming the "peak number 1" and "peak number 2" are ^{10}B and ^{6}Li, respectively. Furthermore, the empty circle and empty square were obtained assuming that the "peak number 2" and "peak number 1" in Fig. 5.4 are ^{10}B and ^{6}Li, respectively. In general, the relative behaviour of the plastic light output for ions in Fig. 5.7-(a) and -(b) is the same.

In order to have a direct comparison with the Horn measurement, the plastic light output difference of ions and protons which is normalised by the plastic light output for ions is depicted in Fig. 5.8. As can be seen, the relative behaviour of the plastic light output in both measurements for ^{3}He, ^{7}Li and ^{7}Be is the same with an uncertainty which is less than 2%. In case of ^{2}H the uncertainty is 6%. Still we can not distinguish ^{10}B among "peak number 1" and "peak number 2" in Fig. 5.4. The reason is that by assuming that the "peak number 1" or "peak number 2" is ^{10}B, almost the same relative light output from the plastic scintillator will be obtained (full and empty circles in Fig. 5.8). Figure 5.7-(c) and (d) shows the pure CsI(Tl) light output of our data (d) and that of Horn (c). In Fig. 5.7-(c), the light output of CsI(Tl) scintillator from the Horn measurement for ^{10}B and ^{6}Li (cross and empty square, respectively) are shown. Figure 5.7-(d) represents the CsI(Tl) light output of our measurement assuming that the "peak number 1" and "peak number 2" in Fig. 5.4 are ^{10}B and ^{6}Li (full circle and empty square), respectively. In addition, the empty circle and full square show the results when assuming that the "peak number 2" and "peak number 1" in Fig. 5.4 are ^{10}B and ^{6}Li, respectively. The star in Fig. 5.7-(b) and -(d) shows the plastic and CsI(Tl) light output of the Heavy ion detector in case the "peak

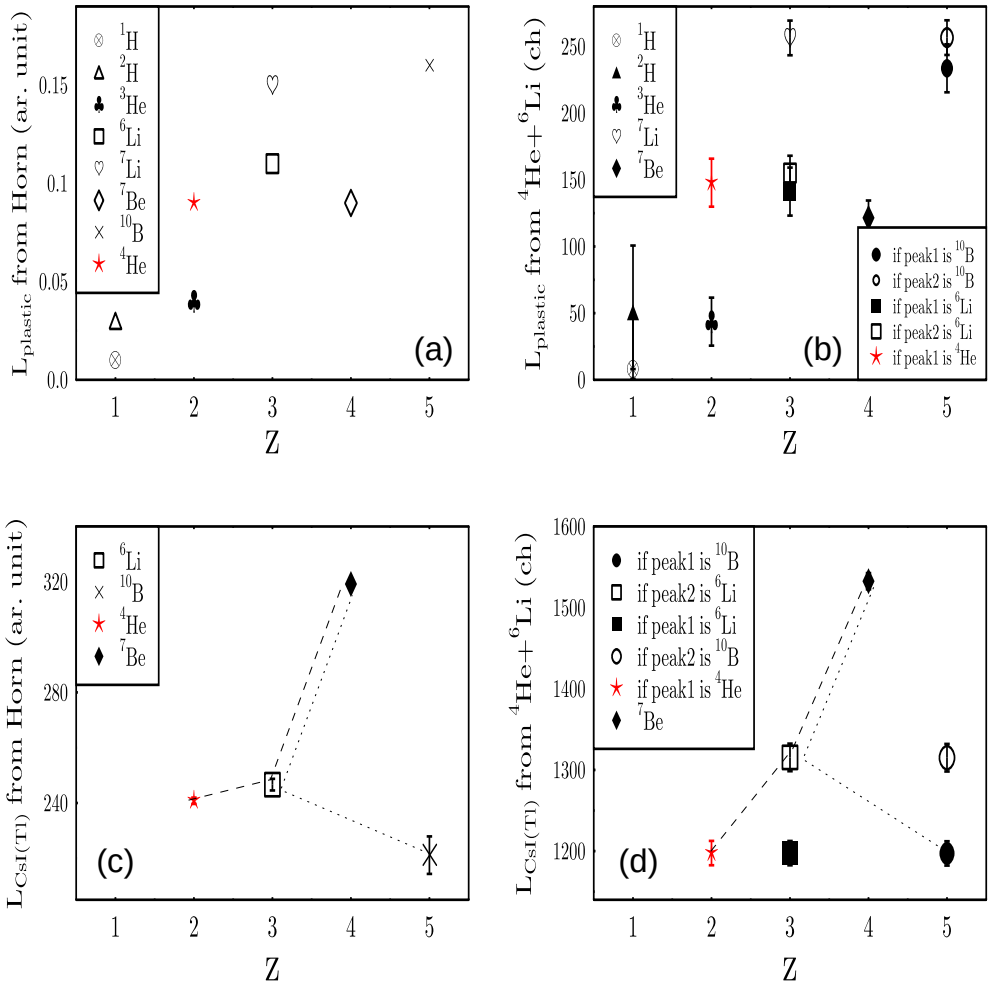

Figure 5.7: Detector light output and identification of the fusion product. (a) and (c): The plastic and CsI(Tl) light output of the produced ions in the ^{6}Li(^{4}He,π^{0})^{10}B* reaction using Horn calibration factors [60, 61]. (b) and (d): The plastic and CsI(Tl) light output of the produced ions using the AGOR facility.

number 1" would be identified as ^{4}He. By comparing the relative positions of the different ions in Fig. 5.7-(c) and Fig. 5.7-(d), we must conclude that the full circle in Fig. 5.7, which belongs to "peak number 1" in the pulse shape of the Heavy Ion detector (Fig. 5.4), is ^{10}B. Furthermore, in Section 5.3.2, it will be explained that the momentum distribution of the "peak number 1" in the Heavy Ion pulse-shape spectrum covers the same range as the momentum distribution of ^{10}B from the Monte-Carlo simulations. All other ions show a random momentum distribution in the range covered by the spectrometer. The "peak number 2" in Fig. 5.4 corresponds to ^{6}Li.

As was mentioned in chapter 1, another pionic fusion experiment using the same experimental setup with an 85.3 AMeV ^{3}He beam on a 130 mg/cm^{2} liquid ^{4}He target has been performed at KVI [43]. Since Time Of Flight information was enough to identify all the produced ions in that experiment, we decided to use that data as a useful tool to have

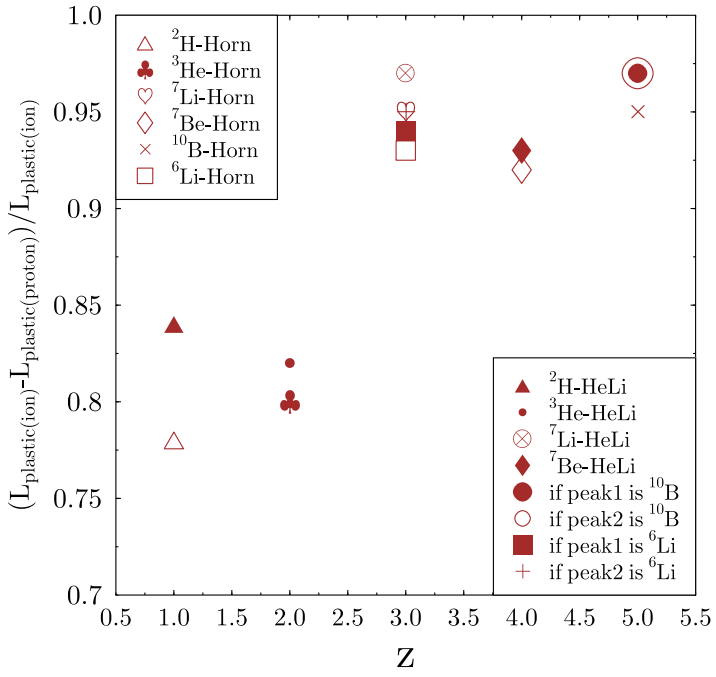

Figure 5.8: The light output of the plastic scintillator for ions divided by the light output for protons plotted as function of ion charge.

one more proof in the identification of ions. In order to compare the light output of detectors in two different reactions, the particle energy should be the same in both reactions. This means that the same settings of the BBS magnetic field in both reactions should be compared. The measured data related to the BBS magnetic fields of 0.9690 Tm and 0.9783 Tm, corresponding to ^{6}Li(^{4}He,π^{0})^{10}B* and ^{4}He(^{3}He,π^{0})^{7}Be reactions, respectively, were selected. There is a 1% difference between the chosen magnetic field strengths of the two reactions, which is equivalent to a shift by about one Heavy Ion detector unit when comparing the ^{6}Li(^{4}He,π^{0})^{10}B* reaction with the ^{4}He(^{3}He,π^{0})^{7}Be reaction (Fig. 5.13). In comparison of the two reactions this detector shift was taken into account. ^{1}H and ^{3}He from the ^{6}Li(^{4}He,π^{0})^{10}B* reaction were selected as reference particles and in order to have the same channel difference between ^{1}H and ^{3}He in two reactions, a gain factor for every Heavy Ion detector module was calculated. Also to shift the channel number of the ^{3}He particle in the ^{6}Li(^{4}He,π^{0})^{10}B* reaction into the same channel number of that particle in the ^{4}He(^{3}He,π^{0})^{7}Be reaction, an offset factor for every Heavy Ion detector module was calculated. Figure 5.9 shows the result of the gain-matched light output of the ^{6}Li(^{4}He,π^{0})^{10}B* experiment in comparison to the light output of the ^{4}He(^{3}He,π^{0})^{7}Be experiment. As result, the peak positions of the known particles like ^{2}H, ^{7}Li and ^{7}Be in both datasets are in agreement for all the Heavy Ion detector modules. The gain-matched peak

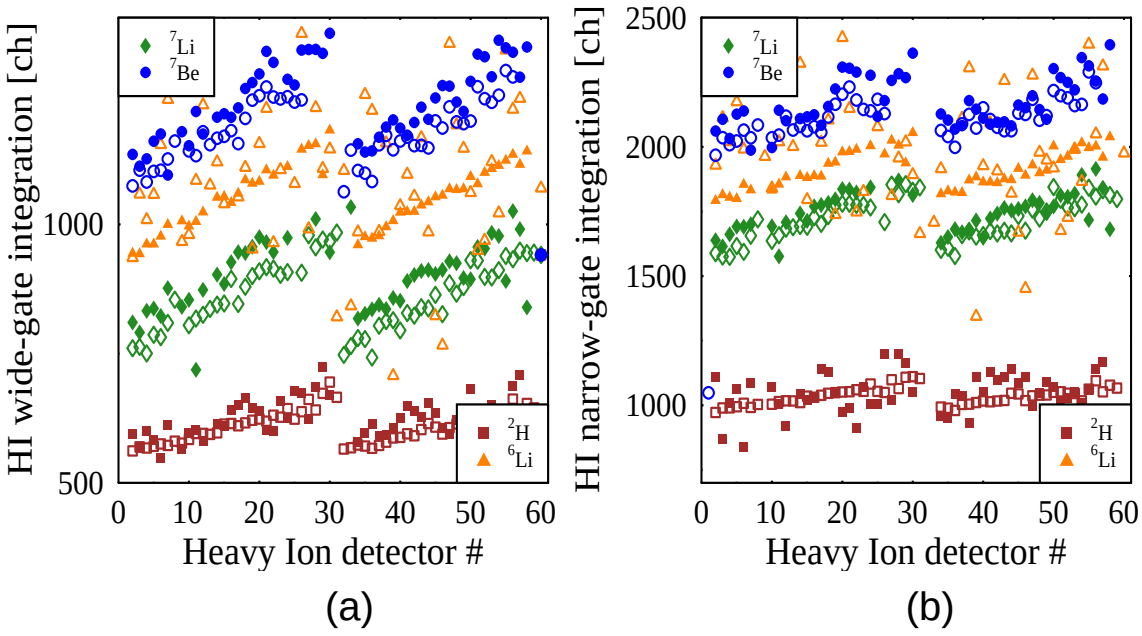

Figure 5.9: (a) ((b)): The empty markers are the light output of the Heavy Ion detector modules for different ions after the wide-gate (narrow-gate) integration for the ^{4}He(^{3}He,π^{0})^{7}Be reaction. The full markers are the light output of the Heavy Ion detector modules after the wide-gate (narrow-gate) integration for different ions in the ^{6}Li(^{4}He,π^{0})^{10}B reaction when the ion peak position is adjusted in gain to the positions of the same ion in the ^{4}He(^{3}He,π^{0})^{7}Be reaction.

position of the particle which is called peak number 2 in Fig. 5.4 for the ^{6}Li(^{4}He,π^{0})^{10}B* reaction, covers almost the same region as ^{6}Li in the ^{4}He(^{3}He,π^{0})^{7}Be reaction. Large fluctuations for ^{6}Li are due to the very low statistics and the difficulty in determining the peak position in the ^{4}He(^{3}He,π^{0})^{7}Be reaction.

Summarising, we conclude that we have confirmed the unique identification of ^{10}B by three different methods.

5.3 Calibration

The calibration of the data is a process in which the recorded (measured) values are identified and associated with physics processes that cause them. By knowing this relation we can actually give a physical meaning to the data stream.

5.3.1 Time calibration

Time calibration of the Plastic Ball and the Inner Shell

The first step in the calibration of the TDC information was a time matching of all the Plastic Ball detectors together. We have used the Plastic Ball-single trigger for the time matching of the Plastic Ball modules. Furthermore, using 600 ns time difference due to the wire lengths which are travelled by one or the other copy of the same signal, the

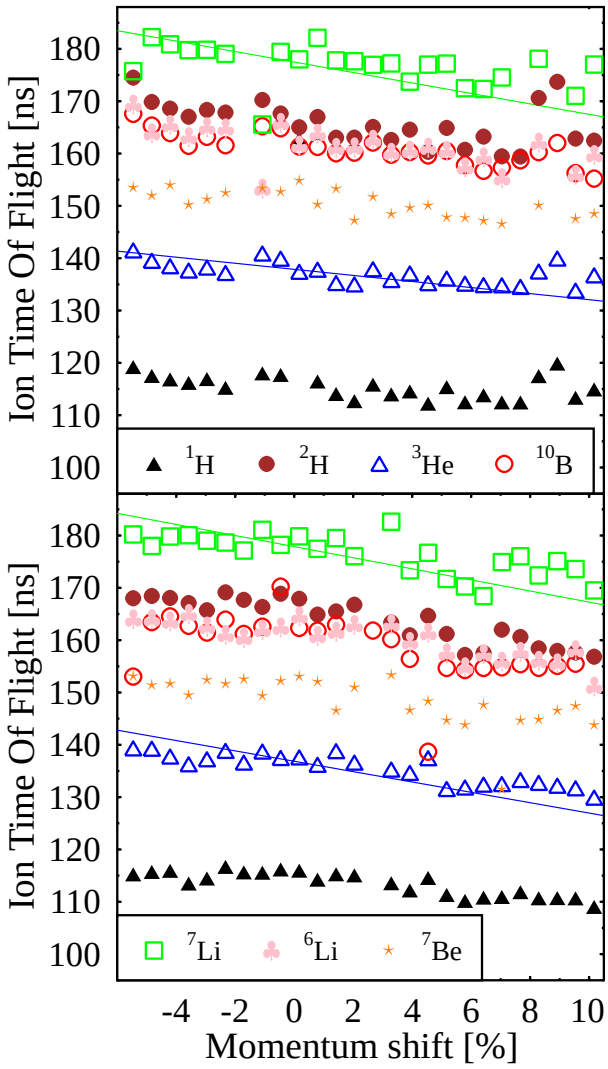

Figure 5.10: Calibration of the ion Time Of Flight from the target to the Heavy Ion detector while passing the BBS. (a) and (b) show the calibrated Time Of Flight measured by the upper and lower row of the HI detector, respectively. The curves are the result of fitting Eq. 5.1 to the Time Of Flight of ^{3}He and ^{7}Li ions.

Plastic Ball TDCs were calibrated. For the time calibration of the Inner Shell modules the same method was applied. The calibrated time signals summed over all the Plastic Ball detectors and all the Inner Shell detectors were already shown in Fig. 5.2.

Calibration of the ion Time Of Flight

In the Time Of Flight information of the Heavy Ion detector, there are two self-triggered peaks originating from the Heavy Ion signals in the single and coincidence modes of the data acquisition (see Fig. 4.8). The relative time of the TDCs was calibrated using these

self-triggered peaks separated by a fixed time delay. A reference detector was chosen and, in order to have the same number of channels between the two triggered peaks in every detector and in the reference detector, a gain factor was calculated. In addition, the first triggered peak for all the detectors was shifted into the same channel of that peak in the reference detector. In this way for every detector the gain and offset factors were calculated. As we expect and as can be seen in Fig. 5.10, with increasing particle momentum the Time Of Flight of all particles decreases. That is because by increasing the particle energy, the particle not only becomes faster but also bends less in the magnetic field and the trajectory length of the particle from the target to the Heavy Ion detector decreases. As result according to Eq 5.1 the particle Time Of Flight decreases. Moreover, by increasing the m/q ratio, in general, the Time Of Flight of different ions with the same momentum increases. By fitting Eq. 5.1 to the calibrated Time Of Flight for every ion, it was found that by increasing the m/q ratio the slope of the fitted curves increases correspondingly (see Table 5.1). The fluctuations with respect to the fitted curves are in the order of a few ns.

Table 5.1: The slope of the fitted curves to the ion Time Of Flight measured by the upper row of the Heavy Ion detector.

Ion	^{1}H	^{3}He	^{7}Be	^{2}H	^{10}B	^{6}Li	^{7}Li
A/Z	1	1.5	1.75	2	2	2	2.33
Slope	-0.40 ±0.03	-0.58 ±0.03	-0.56 ±0.04	-0.71 ±0.03	-0.9 ±0.03	-0.99 ±0.04	-1. ±0.04

5.3.2 Energy calibration

Momentum calibration in the Heavy Ion array

Since the Heavy Ion module position gives us the momentum of the detected ion, we have a useful observable to calculate the ion energy. The energy calibration of the individual Heavy Ion detectors is not necessary. In the magnetic field, charged particles move in a bent trajectory. The radius of the trajectory, ρ, is linearly related to the momentum of the particle, $p = mv$ by

$$B\rho = mv/q, \tag{5.5}$$

where B, q and m are magnetic field strength, charge and particle mass, respectively. The quantity $B\rho$ is called magnetic rigidity. The deviation of the rigidity of a particle with respect to the particle travelling along the central ray of the spectrometer with trajectory radius ρ_0 is defined as

$$\Delta p/p_{central} = \frac{B\rho - B\rho_0}{B\rho_0} \tag{5.6}$$

By adjusting the quadrupole- and the dipole-field strengths, particles can be positioned and bent in a certain direction in the Big-Bite Spectrometer (Fig. 4.1). During the experiment, the magnetic field was set such that ^{10}B with $E = 93$ MeV hits the middle of the Heavy Ion array. This setting is called the nominal setting of the Big-Bite Spectrometer for the present experiment and the corresponding values are shown in Table 5.2.

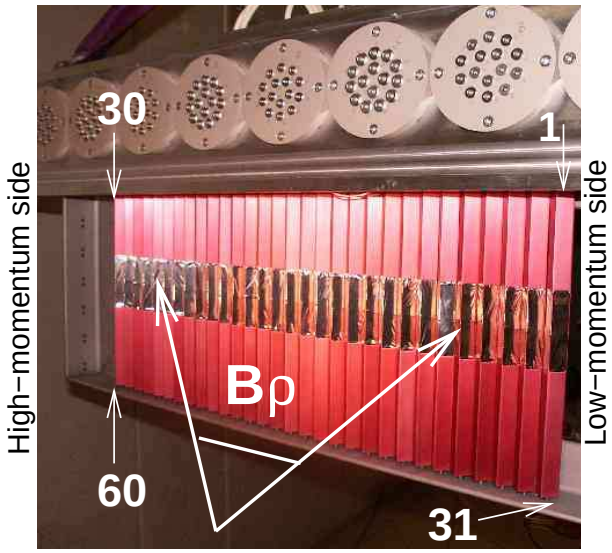

Figure 5.11: Schematic relation between the rigidity and the detector position in the Heavy Ion detector array. The numbering sequence of detectors from 1-30 and 31-60 is indicated. The low- and high-momentum sides of the array are depicted in the figure.

Table 5.2: The experimental values of the Big-Bite Spectrometer for the nominal rigidity setting. Using these values, ^{10}B with $E = 93$ MeV hits the centre of the Heavy Ion detector array.

current of the dipole	222.576 A
current of the first quadrupole	117.270 A
current of the second quadrupole	139.644 A
rigidity	0.8809 Tm

Suppose we have a group of the same kind of particles with different energies and apply dipole and quadrupole magnetic fields in the specific magnet setting of the Big-Bite Spectrometer. If the particles pass through the magnetic field, particles with different energies will hit Heavy Ion detector modules in different positions of the array.

Equivalently, if we have a group of the same kind of particles with the same energies and apply BBS magnetic fields in different settings, by changing the magnetic field the momentum of the particle will change and they will be detected at different detector position. In one setting of the Big-Bite Spectrometer detector 'x' will be hit, while in another setting, detector 'y' will detect the particle. Since the particle energy is the same in both settings, the energy deposition in detectors 'x' and 'y' should be the same. We used this fact for the momentum calibration of the Heavy Ion detector array also for the gain matching of the Heavy Ion detectors.

In commissioning runs for the Heavy Ion detectors, we have performed a test experiment with various projectiles (^{4}He, ^{16}O, ^{12}C, ^{20}Ne) at laboratory energy of 14.3 AMeV on ^{197}Au and ^{12}C targets and measured the elastic peak. The aim was to study the response to the different ion species and the particle identification capability. As result, the elastic peak was mainly found in one detector module with a small contribution of the neighbour-

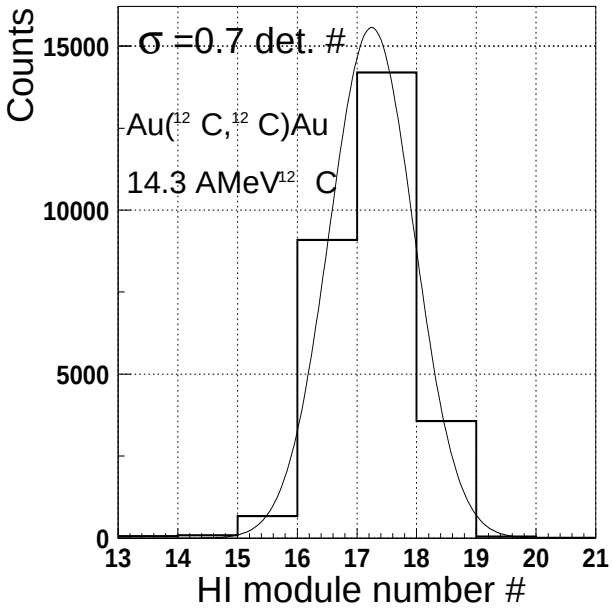

Figure 5.12: Heavy Ion detectors in the Heavy Ion detector array which are associated with the energy deposition of one particle from the elastic interaction.

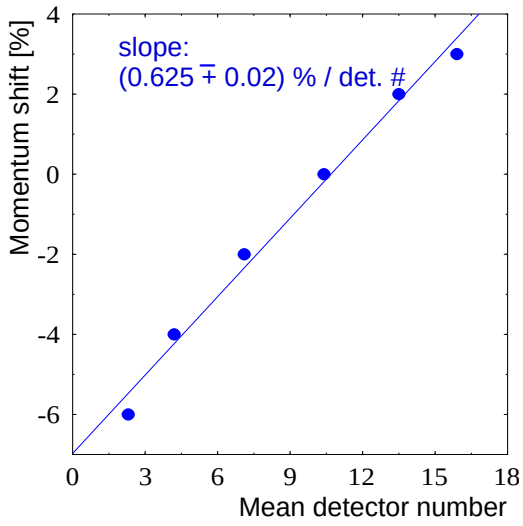

Figure 5.13: Momentum shift measured by detector position in the Heavy Ion array.

ing detectors (Fig. 5.12). The horizontal position resolution was about 21 mm FWHM which is equivalent to 1.6 detector units, where the horizontal detector bin size is 13 mm. The horizontal position resolution is mainly determined by the acceptance of the Big-Bite Spectrometer (see Section 5.6). The mean detector position has been correlated with a momentum shift introduced by the magnetic field setting with respect to the setting for the central ray. Figure 5.13 shows the relation between the momentum shift in % and the

mean detector position. As can be seen, a good linearity with the slope of 0.625%/detector unit has been obtained.

Gain matching of the light output for the Heavy Ion detector

During the pionic fusion experiment, data were taken with the nominal setting of the BBS ($\Delta p/p_{central}$ =0%). A small amount of data was taken with the momentum deviations $\Delta p/p_{central}$ of -10%, -5%, 5% and 10% with respect to the central momentum $p_{central}$ of the nominal setting. These data were used to study the response of the Heavy Ion detector array to various ion masses, energies and momenta in order to calibrate the array. The negative value of the momentum or rigidity deviations implies the stronger magnetic field of the Big-Bite Spectrometer. After the experiment these data were used for the calibration. As is shown in Fig. 5.13, by changing the momentum of the particle by 0.625% with respect to the central momentum, the hit Heavy Ion detector will be shifted by one unit. Equivalently, the rigidity change of a particle at 0% and 5% rigidity settings, is equivalent to a shift by 8 detector units. Therefore in different settings, there are "equivalent detectors" with the same light output, e.g. 'HIdet', 'HIdet + 8', 'HIdet + 16' and 'HIdet + 24' with $\Delta p/p_{central}$=-10%, -5%, 0% and 5%, respectively. For the gain matching of the Heavy Ion detectors, four detectors were chosen as "equivalent detectors". In addition, the 'HIdet + 16' in the $\Delta p/p_{central}$=0% setting, positioned around the middle of the array, was chosen as reference detector. ^{3}He and ^{10}B were chosen as reference particles.

In the first step of the gain matching procedure, by calculating a gain factor for every "equivalent detector", the same channel difference as found in the reference detector between the ^{3}He peak position and the ^{10}B peak position, was obtained

$$gain(HIdet) = \frac{L_{^3He,rig0}(ref) - L_{^{10}B,rig0}(ref)}{L_{^3He,rig-10}(HIdet) - L_{^{10}B,rig-10}(HIdet)}, \tag{5.7}$$

$$gain(HIdet+8) = \frac{L_{^3He,rig0}(ref) - L_{^{10}B,rig0}(ref)}{L_{^3He,rig-5}(HIdet+8) - L_{^{10}B,rig-5}(HIdet+8)}, \tag{5.8}$$

$$gain(HIdet+24) = \frac{L_{^3He,rig0}(ref) - L_{^{10}B,rig0}(ref)}{L_{^3He,rig+5}(HIdet+24) - L_{^{10}B,rig+5}(HIdet+24)}, \tag{5.9}$$

where 'ref' indicates the reference detector. $L_{^3He,rig0}(ref)$ indicates the light output of the reference detector which has been measured for the ^{3}He particle in the central momentum (rigidity) $p_{central}$ of the nominal setting. Furthermore, to have the ^{3}He peak in the same position as the ^{3}He peak in the reference detector, an offset for every "equivalent detector" was calculated

$$offset(HIdet) = L_{^3He,rig0}(ref) - gain(HIdet) \times L_{^3He,rig-10}(HIdet), \tag{5.10}$$

$$offset(HIdet+8) = L_{^3He,rig0}(ref) - gain(HIdet+8) \times L_{^3He,rig-5}(HIdet+8), \tag{5.11}$$

$$offset(HIdet+24) = L_{^3He,rig0}(ref) - gain(HIdet+24) \times L_{^3He,rig+5}(HIdet+24). \tag{5.12}$$

The second step was to use the derived gain factors and the offsets to calculate the calibrated channel number of all other particles in all the BBS magnet settings for the

"equivalent detector" as follows:

$$gL_{j,k}(i) = L_{j,k}(i) \times gain(i) + offset(i). \tag{5.13}$$

$gL_{j,k}(i)$ and $L_{j,k}(i)$ are the light output of the detector "i" after and before the gain matching, respectively, when particle "j" in the rigidity deviation setting of "k" hits the detector "i".

The third step was to calculate the gain factors and the offsets for the rest of the detectors. These detectors are called "middet" and are positioned between every two "equivalent detector". The gain-matched "equivalent detector" were used to gain match the rest of the detectors. The light output of a detector is proportional to the particle momentum as follows:

$$L \propto E = \frac{p^2}{2m}, \tag{5.14}$$

where

$$\frac{p^2}{2m} \propto (horizontal\ module\ position\ in\ the\ Heavy\ Ion\ detector\ array)^2. \tag{5.15}$$

L is the detector light output. E, p and m are the particle kinetic energy, particle momentum and the particle mass, respectively. According to Eq. 5.14 and 5.15, by moving from a Heavy Ion detector module to the neighbouring one in the array, the light output does not change linearly. The calibrated light output of the four "equivalent detectors" for the reference particles in the central rigidity $p_{central}$ of the nominal setting were fitted to equation $y = ax^2 + b$. By using the resulting fitting coefficients a and b and the proper detector number x (which is a number proportional to the horizontal module position in the Heavy Ion detector array), the gain-matched light output of the rest of the detectors in the array for ^{3}He and ^{10}B was calculated. Finally, the gain and the offset factors for the rest of the detectors were obtained

$$gain(middet) = \frac{gL_{^3He,rig0}(middet) - gL_{^{10}B,rig0}(middet)}{L_{^3He,rig0}(middet) - L_{^{10}B,rig0}(middet)}, \tag{5.16}$$

$$offset(middet) = gL_{^3He,rig0}(middet) - gain(middet) \times L_{^3He,rig0}(middet). \tag{5.17}$$

These two values allowed the gain matching by shifting all the ions for the specific detector into the correct channel number. These steps were applied for the modules in the upper row of the Heavy Ion detector array (detector 1-30) and for the gain matching of the total light output (plastic+CsI(Tl)) and the plastic light output separately. The gain matching of the modules positioned in the lower row (detector 31-60) was achieved by comparison to modules that have the same horizontal position but are placed in the upper row. A gain and an offset factor were calculated to move the ^{3}He and ^{10}B peak positions to the same channel numbers as the ^{3}He and ^{10}B peak positions in the upper module.

The calibrated total and plastic light output of the Heavy Ion detectors for all particles in all the measured rigidities before and after the gain matching are shown in Figs. 5.14 and 5.15, respectively. The graphs in the left column depict the peak position of the particles before the gain matching. The graphs in the right column are representing the calibrated peak positions. From the top to the bottom of Figs. 5.14 and 5.15, the results

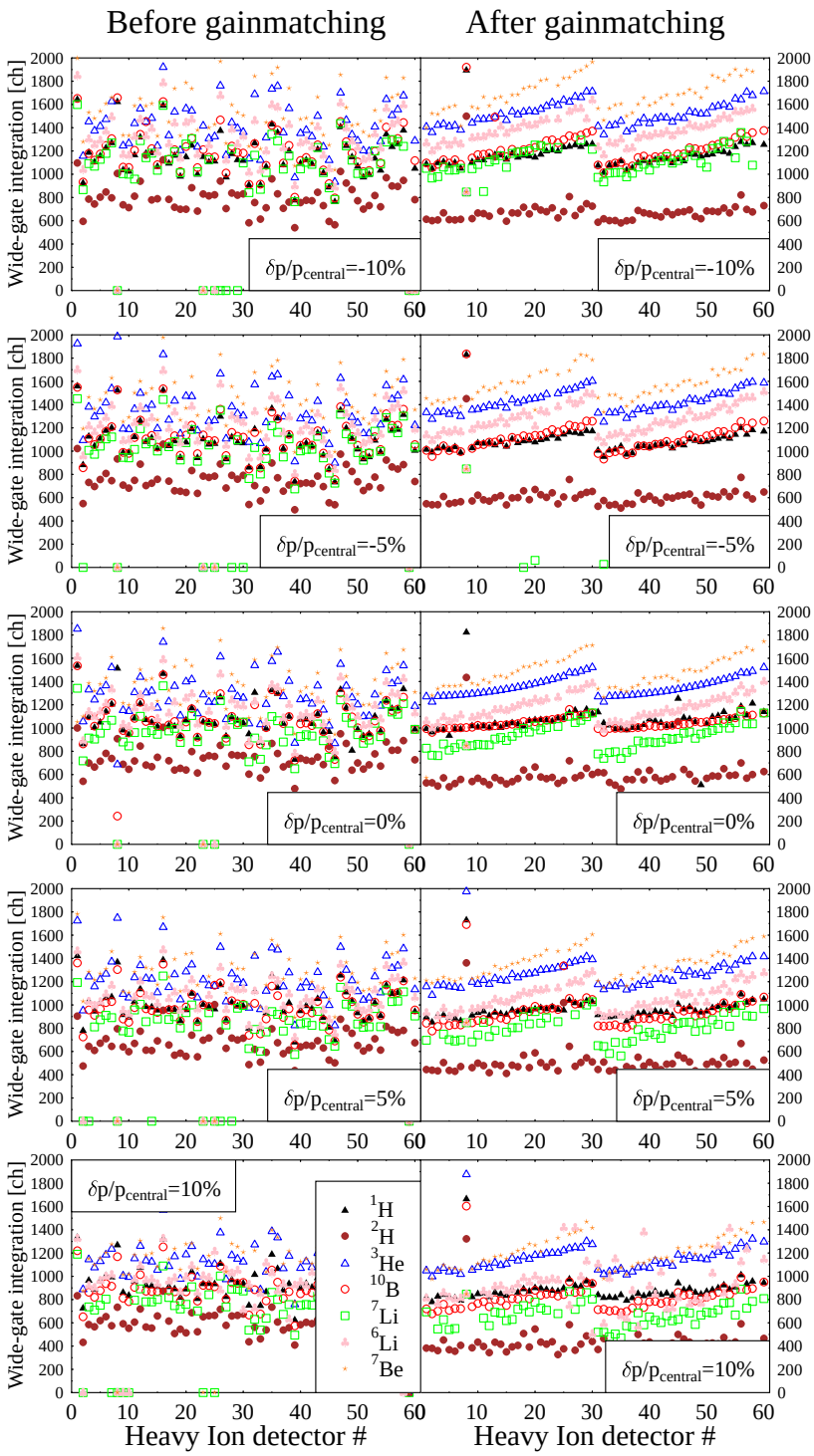

Figure 5.14: Gain matching of the ion light output from the wide-gate integration in the different rigidity deviations with respect to the central ray. Left (Right) figures correspond to the ion peak position in the spectrum of the wide-gate integration before (after) gain matching of the detectors. Different markers are representing different ions. The rigidity deviations from the central ray from the top to the bottom graphs are -10%, -5%, 0%,5% and 10%, respectively.

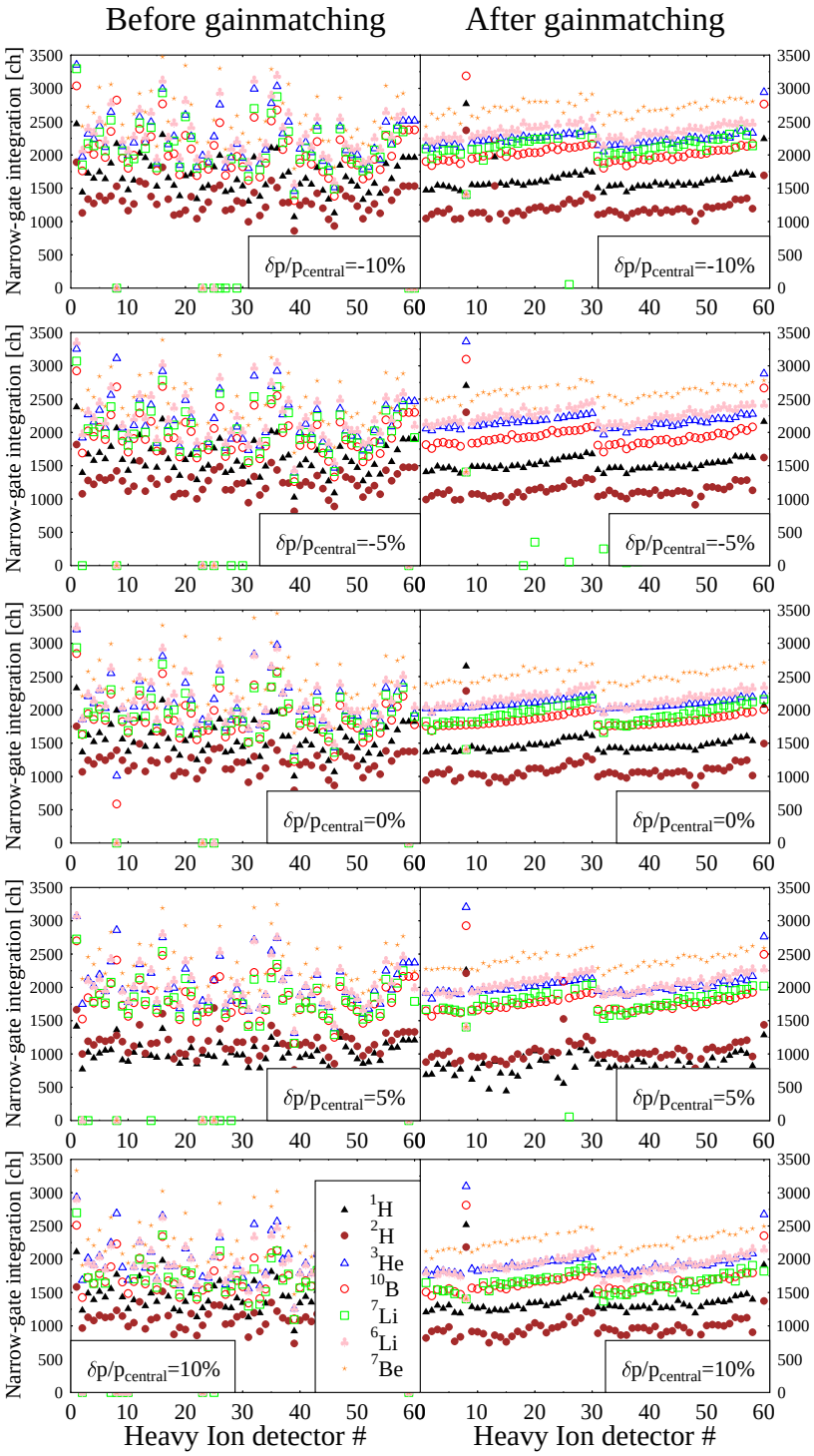

Figure 5.15: Gain matching of the ion light output from the narrow-gate integration in the different rigidity deviations with respect to the central ray. Left (Right) figures correspond to the ion peak position in the spectrum of the narrow-gate integration before (after) gain matching of the detectors. Different markers are representing different ions. The rigidity deviations from the central ray from the top to the bottom graphs are -10%, -5%, 0%, 5% and 10%, respectively.

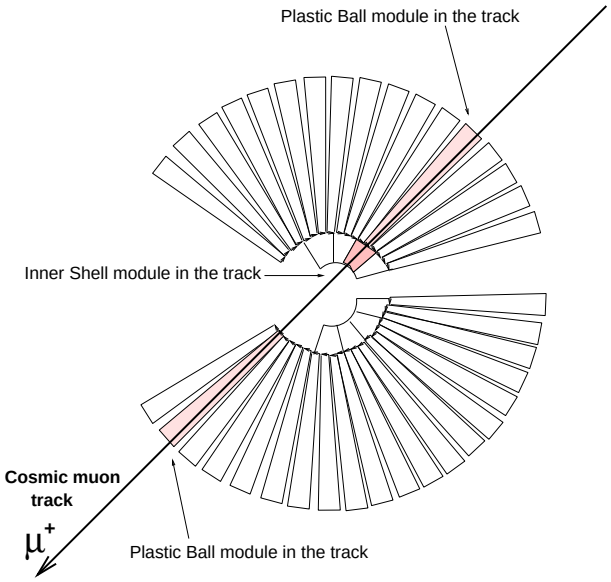

Figure 5.16: Sketch of a muon track to calibrate the Plastic Ball and the Inner Shell modules.

of the measurements using the momentum (rigidity) deviations $\Delta p/p_{central}$=-10%, -5%, 0%, 5% and 10% are shown. Furthermore, different symbols correspond to the different particles. The points which are completely off correspond to the detector modules which were not properly operating (two detector modules) and were not used for the further analysis.

As can be seen, after the gain matching using the two particles (^{3}He and ^{10}B) a smooth behaviour of the light output in the Heavy Ion detector array for all the other particles is obtained. This implies the existence of a systematic correlation between the modules of the Heavy Ion array. According to Eq 5.14, since p is proportional to the horizontal position of the ion in the Big-Bite Spectrometer or the x-axis in Figs. 5.14 and 5.15, the slope of the lines is proportional to the particle mass. Thus, the positive slope of the lines is expected and implies that the light output of the modules positioned on the higher momentum-side of the Heavy Ion detector array is higher than the light output of the modules positioned on the lower momentum-side. In addition, by decreasing the magnetic field strength, in general, the light output decreases which is the result of the lower particle energy. This result is shown on the right side of Figs. 5.14 and 5.15. A detailed analysis of the dependence of the detector light output on particle type and detector material, including the quenching effect, is in progress and will be reported in another thesis [43].

Energy calibration of the Inner Shell and the Plastic Ball backward hemisphere

To convert the light output measured by the ADCs into energy units for the Inner Shell and the Plastic Ball modules, the signal from high energy cosmic muons was exploited. For the calibration only tracks of cosmic muons that pass the centre of the Plastic Ball were chosen. The track of a muon in the cosmic data was chosen such that the muon passes

one Plastic Ball module, the Inner Shell module behind it and the corresponding Plastic Ball module opposite to the first one (Fig. 5.16). In addition, in order to exclude random coincidences and those of cosmic muon events which don't pass through three different detectors longitudinally, one more condition in the track selection has been applied. The condition was that a cosmic muon event is selected only if the closest 12 neighbours of the mentioned Plastic Ball modules in the track have not given a signal. The same condition for the closest 6 neighbours of the Inner Shell module in the track was applied. This sharp track definition for the Plastic Ball and the Inner Shell modules generated the clearest cosmic peak. A Monte-Carlo simulation for 1 GeV muons was performed to simulate minimum ionising particles. Muons were produced on the surface of a virtual hemisphere, centred in the centre of the Plastic Ball detector, with radius of 1500 cm. Muon tracks in the Plastic Ball and in the Inner Shell modules were selected under the same conditions as applied for the measured data. The calibration was performed by matching the measured peak positions to the peak positions from the simulation.

Due to the zenith angle distribution of cosmic muons, some of the almost horizontally oriented Plastic Ball modules, (about 20% of the total), and the Inner Shell modules that are positioned behind them, reveal a rather broad cosmic peak. Because of the almost cubic geometry, the energy deposition of the cosmic muons in the Inner Shell modules is independent of the angle of incidence. Even if the tracks are not well defined, cosmic muons deposit almost the same amount of energy with a clear peak. Therefore, to calibrate the horizontally oriented Inner Shell modules, vertical cosmic muons were used. For the horizontally positioned Plastic Ball modules, a cross calibration with respect to the neighbouring modules using photons in the pionic fusion data was done.

Figure 5.17-(a) and -(b) shows the energy deposition of cosmic muons inside the Plastic Ball module (plastic plus CaF_2 scintillators) and inside the plastic scintillator, respectively, summed over all the modules. The measured and calibrated (solid curve) energy deposition of the cosmic muons in the Plastic Ball modules shows peaks around 74 MeV and 72 MeV with the resolution of 38% FWHM and 40% FWHM for the total deposited energy and for the energy deposition in the plastic scintillators, respectively. The muon peaks in the simulated results shown by the dotted curves are at the same positions as the experimental data but the peaks have different widths compared to the measured peaks. This difference in the peak widths is the result of the incomplete shower collections inside the scintillators which have not yet been taken into account accurately enough in the simulation. In particular, threshold effects for light production by low energy particles and light absorption at the module boundaries were not modelled in all details. In order to match the energy resolution of the detectors for the simulated and measured cosmic muons and correct for the incomplete shower collection, the simulated muon energy depositions inside the plastic plus CaF_2, plastic and CsI(Tl) scintillators were multiplied by three different factors as Gaussian random deviates. The simulated results of the cosmic muon energy deposition after the correction for the absorption in the module, is shown in Fig. 5.17 by the dashed curves. It should be mentioned that the obtained factors work well to match the energy resolution of the detectors for the simulated and measured photons from π^0 decay in the ^{6}Li(^{4}He,π^{0})^{10}B* reaction. Therefore, to simulate the ^{6}Li(^{4}He,π^{0})^{10}B* reaction and the detector responses, the same factors have been employed.

Using cosmic muons, we have calibrated the total light output of the Plastic Ball modules. Because the cosmic muons deposit a very low energy in the CaF_2 scintillator

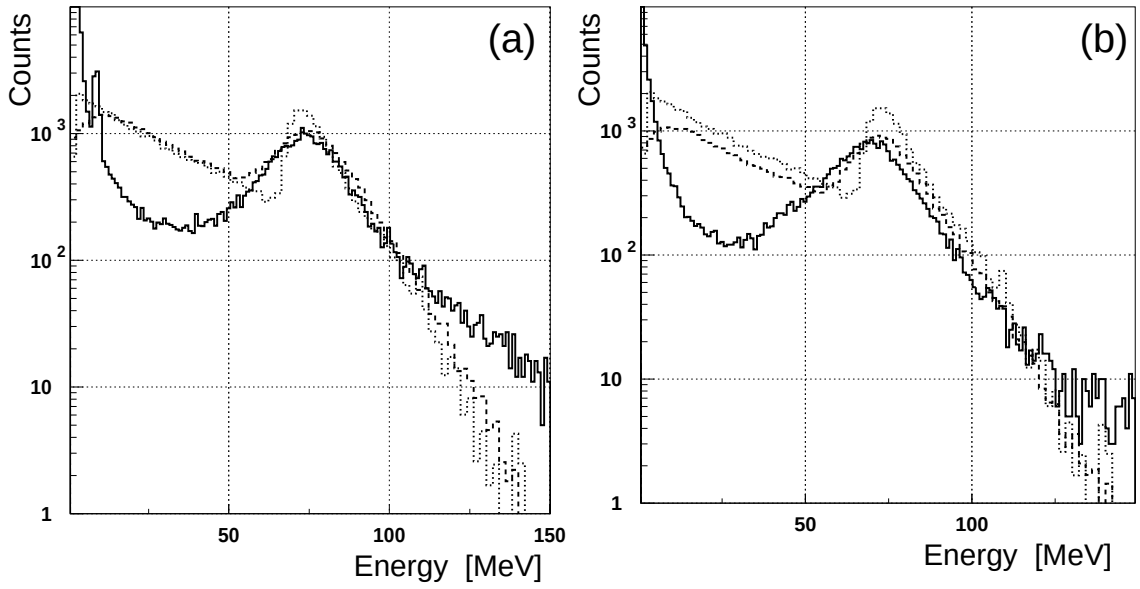

Figure 5.17: Cosmic muon energy deposition in a complete Plastic Ball module (a) and in the plastic scintillator only (b), summed over all modules. Solid curves are representing the measured results. The dotted and dashed curves show the simulated results before and after applying the smearing effects on the energy resolution, respectively.

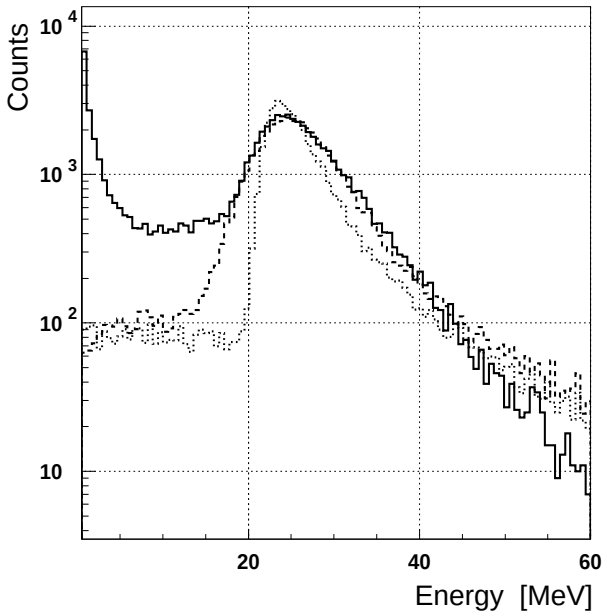

Figure 5.18: Cosmic muon energy deposition in the CsI(Tl) scintillators, summed over all modules. The solid curve is representing the measured result. The dotted and dashed curves show the simulated results before and after applying the smearing effects on the energy resolution, respectively.

(less than 3% of the total deposition), in the pulse shape of the Plastic Ball (Fig. 5.3), cosmic muons are found around the diagonal line. In Fig. 5.17-(b), there is still a difference between the peak position of the simulated and the measured muon energy depositions (solid and dotted curves) inside the plastic scintillators. The reason is that the same calibration factors which were obtained for the total light output, were used to calibrate the plastic light output. In this way the deposited energy of the cosmic muons inside the CaF_2 scintillator was not considered. Since for the further analysis only the total light output of the photons is used, an exact calibration for the plastic light output is not necessary.

Figure 5.18 represents the measured (solid curve) and the simulated (dashed and dotted curves) energy deposition of cosmic muons inside the Inner Shell modules, summed over all the modules. The calibrated measured (solid curve) energy deposition of the cosmic muons in the Inner Shell module shows a peak around 25 MeV, with the resolution of 38% FWHM. The dotted and dashed curves are the simulated results before and after applying the smearing effects on the energy resolution, respectively.

Energy calibration of the Plastic Ball forward hemisphere

For the gain matching of the Plastic Ball modules in the forward direction ($\theta_{module} < 90°$), high energy protons from ^{6}Li breakup in the pionic fusion experiment were used. According to the Monte-Carlo simulations, protons with energies less than 32 MeV deposit all their energy inside the CaF_2. At energies above 32 MeV, protons punch through the CaF_2 and enter the plastic module (Fig. 5.19-(a)). For all the forward Plastic Ball modules, the punch-through point can be clearly identified in the pulse shape spectrum (Fig. 5.3). That point was used to gain match all the Plastic Ball modules positioned in the forward direction. After the gain matching, the same method as described above for the calibration of the backward direction with cosmic muons was used to calibrate one Plastic Ball module in the forward direction. The calibrated proton punch through point in the pulse shape spectrum of that module was used to calibrate the rest of the modules including the horizontally oriented detectors in the forward direction. It should be mentioned that due to the fact that protons with energies less than 120 MeV deposit all their energy inside the Inner Shell detectors (Fig. 5.19-(b)) and can not reach the Plastic Ball detectors, which are placed behind the Inner Shell, it was not possible to use the proton punch-through point to gain match the backward part of the Plastic Ball.

5.4 Candidate selection

5.4.1 Clustering of the Plastic Ball detectors

According to Monte-Carlo simulations, the produced photons from π^0 decay do not only deposit energy into one single Plastic Ball module, but will share some energy with the neighbouring modules. In order to determine the full deposited energy, we need to form a cluster of relevant detectors and determine the total signal in the cluster. A cluster is the largest possible group of adjacent Plastic Ball modules in which an energy greater than the ADC threshold was registered. A module is hit whenever its ADC recorded values above the pedestal. The hits in the modules forming a single cluster must be coincident

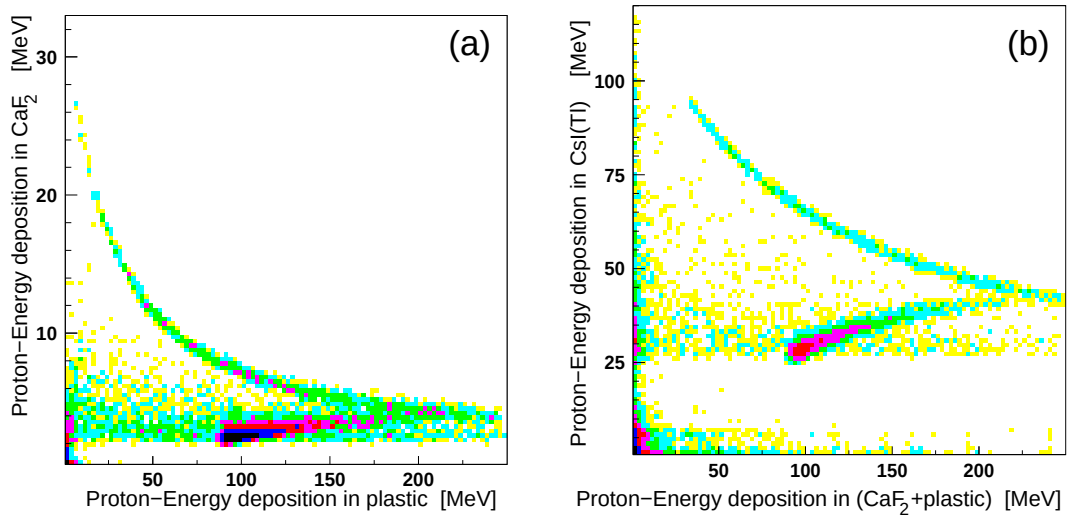

Figure 5.19: (a): The simulated proton energy deposition in the CaF_2 scintillator as a function of energy deposition in the plastic scintillator of the Plastic Ball module. (b): The simulated proton energy deposition in the CsI(Tl) scintillator as a function of energy deposition in the CaF_2 plus plastic scintillator of the Plastic Ball module.

in time. The time window used for this cut ranges from -60 ns to 60 ns. A cluster-finding routine has been employed which scans over all the Plastic Ball modules in order to find the possible candidates. In the first step, if the energy deposition in a Plastic Ball module is larger than the hardware threshold or a suitably defined software energy threshold, a cluster including that module, called the seed module, will be formed. In the next step, the direct neighbours of the seed module will be checked and if they are also hit, they will be recognised as a part of that cluster. In case a hit module is not the direct neighbour of the seed module, that module will be part of another cluster. The cluster-finding routine takes care that in one event every hit module belongs to only one cluster. During the experiment and data analysis, the energy threshold for all the Plastic Ball modules was set just above the pedestal (for more information about the pedestal, see Section 4.9).

Sometimes, energy deposition is caused by a part of an electromagnetic shower which has split off from the main cluster. Then a group of crystals is identified by mistake as a separate cluster even though it should be part of the main cluster. This effect is caused by fluctuations of the electromagnetic shower. If the energy deposited in an individual module is too low and the amount of produced light is insufficient to be detected, such a fluctuation may form a small and low energy cluster close to, but separated, from the main cluster. This wrongly identified cluster is called a "split-off".

The clustering routine was optimised to remove the split-offs. In the second step of the clustering, the routine not only checks the direct neighbours of a hit module but also checks the direct neighbours of the neighbours. The new routine passes the intermediate modules with no deposited energy up to two detector units and collects the next hit module into the same cluster. In order to check the optimised clustering routine, single photon events with E_γ =87 MeV produced in a Monte-Carlo simulation were analysed. Figure 5.20-(a) shows the multiplicity of the Plastic Ball clusters for a single photon, before

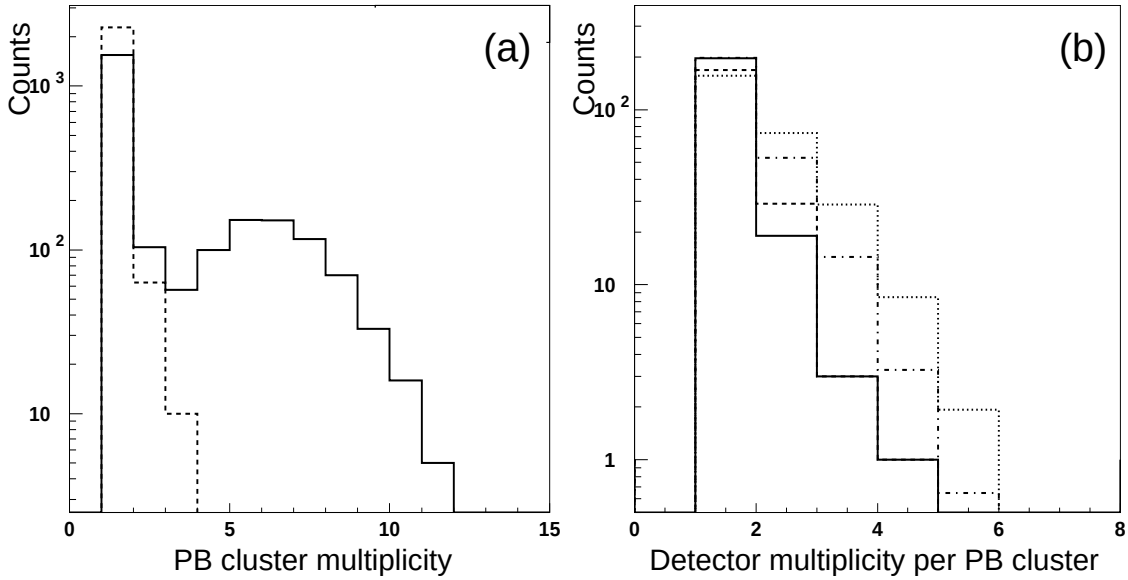

Figure 5.20: (a): The Plastic Ball (PB) cluster multiplicity using the energy deposition of a single photon with E_{γ} =87 MeV produced in the Monte-Carlo simulation. The solid and dashed curves are the results before and after improving the clustering method, respectively. (b): The Plastic Ball detector multiplicity per cluster using the energy deposition of one of the two photons originating from π^{0} decay in the ^{6}Li(^{4}He,π^{0})^{10}B* reaction. The solid and dashed curves are the measured results before and after the optimisation of the clustering method, respectively. The dashed-dotted and dotted curves are the simulated results using the unmodified and modified clustering methods, respectively. The measured and simulated results have been normalised at multiplicity one for the unmodified clustering method.

(solid curve) and after (dashed curve) improving the clustering method. The chance of producing split-offs for an event using the unmodified clustering method has been studied and is 34% (multiplicity≥2 shown by the solid curve in Fig. 5.20-(a)). However, after the modification of the clustering method, the chance of producing split-offs, is reduced to less than 3% (multiplicity≥2 shown by the dashed curve in Fig. 5.20-(a)). Figure 5.20-(b) represents the Plastic Ball module multiplicity in a formed cluster, when the cluster is hit by one of the two photons from π^{0} decay in the ^{6}Li(^{4}He,π^{0})^{10}B* reaction. The solid and dashed curves are the measured results before and after the modification of the clustering method, respectively. For the multiplicity≥2, the dashed curve falls on top of the solid curve. The dashed-dotted and dotted curves are the simulated results using the unmodified and modified clustering methods, respectively. The simulated results of the module multiplicity in one cluster cover the same region as the measured results. After the clustering modification, the multiplicity of the Plastic Ball modules in one cluster has increased. As can be seen, the number of events with two or more detector units per Plastic Ball cluster increases. Consequently, the number of events with one detector unit per Plastic Ball cluster decreases. In fact, while the unmodified clustering routine produces a Plastic Ball cluster with more than two modules in less than 7% of events, this value increases to 15% after the modification of the clustering method. This is the result

of including the split-offs into the main cluster.

Position reconstruction

Photons from π^0 decay hit the Inner Shell and the Plastic Ball detectors. Since the Plastic Ball is a highly segmented detector system, the position information of the Plastic Ball modules has been used to reconstruct the particle position. In order to estimate the direction of the incident particle, three different methods have been investigated. In the first method, the module in the cluster which has maximum energy deposition determines the position of the cluster. Therefore, the rest of the hit modules inside the cluster does not contribute to the cluster position determination. In the second method, the position of the cluster is simply the centre of gravity of the shower:

$$\theta_{calc.} = \frac{\sum_i w_i \theta_i}{\sum_i w_i}, \tag{5.18}$$

$$\phi_{calc.} = \frac{\sum_i w_i \phi_i}{\sum_i w_i}, \tag{5.19}$$

where θ_i and ϕ_i are the polar and the azimuthal angles of the ith individual Plastic Ball module in the cluster, respectively, and the weight factors w_i are taken as the energy E_i deposited in that module. Equivalently, the weights may be viewed as the fraction of the total shower energy in module i, $w_i = E_i/E_T$ with $E_T = \sum_i E_i$. In such a linear way of energy weighting, all the modules inside a cluster equally contribute to the cluster position determination.

In the third method, instead of the weights which are linearly proportional to the deposited energy in a module, logarithmic weights are used as given by the following expression [62]:

$$w_i = \max(0, [W_0 + ln(\frac{E_i}{E_T})]). \tag{5.20}$$

W_0 is a free dimensionless parameter and can be determined from the Monte-Carlo simulations. In case of Plastic Ball, W_0 was calculated and is 3.9. The motivation for this expression with logarithmic weights of the deposited energy in the module is to take into account the exponential falloff of the shower energy distribution.

In order to compare different methods, the response of the Plastic Ball for a single photon has been studied in the Monte-Carlo simulations. In our case, the results of all three methods for the single photon agree within the detector resolution. Figure 5.21 shows the simulated results of the reconstructed position in the Plastic Ball when two photons from π^0 decay in the pionic fusion reaction of ^{6}Li(^{4}He,π^0)^{10}B* were used. Graphs (a) and (b) in Fig. 5.21 are the reconstructed photon polar and azimuthal angles plotted as a function of the incident photon polar and azimuthal angles, respectively. Graphs (c) and (d) in Fig. 5.21 show the projected results of the (a) and (b) panels, respectively, along the diagonal lines. As can be noticed, the resolution (σ) of the angle determination for the polar and the azimuthal angles is 7° and 6°, respectively, which is about equal to the opening angle covered by one detector unit in the Plastic Ball. In Fig. 5.21, the first method of the position reconstruction has been used. Since the resulting angular resolutions of all the three reconstruction methods are the same, the first method was

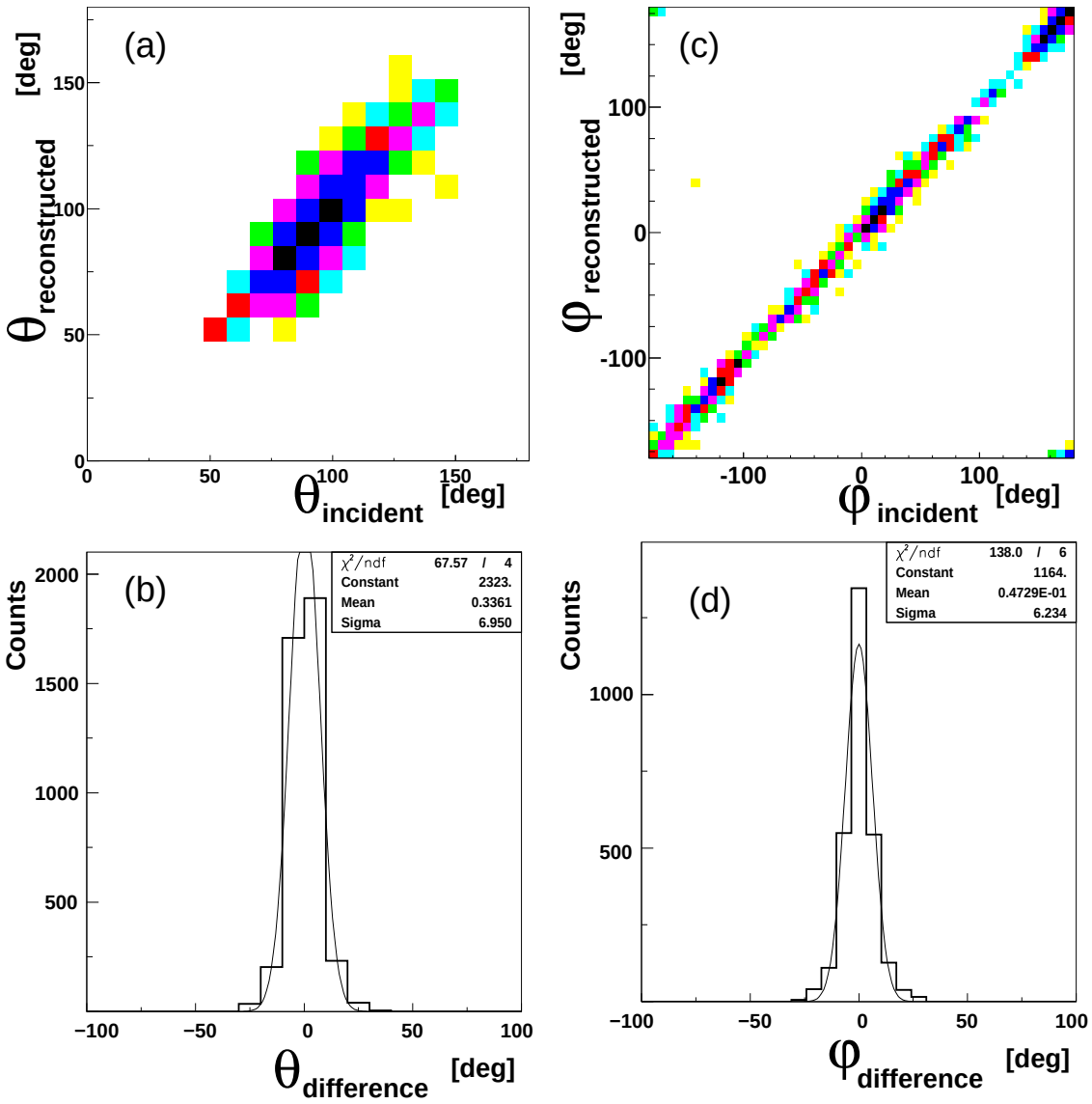

Figure 5.21: Reconstructed and incident angles of the photon with the higher energy from neutral pion decay using the Monte-Carlo simulation of the ^{6}Li(^{4}He,π^{0})^{10}B* reaction. (a) shows the two-dimensional scatter-plot of reconstructed versus incident polar angles. (c) shows the two-dimensional scatter-plot of reconstructed versus incident azimuthal angles. (b) shows the difference of the reconstructed and the incident polar angles. (d) shows the difference of the reconstructed and the incident azimuthal angles.

chosen for the further analysis.

5.4.2 Pion reconstruction methods

In the reaction of interest (^{6}Li(^{4}He,π^{0})^{10}B*), the produced neutral pions immediately decay in the target into two photons with large opening angle as expected from two-

photon decay of π^0's moving with small velocity in the laboratory. In the experiment, the polar and azimuthal angles of both photons from the π^0 decay, the energy deposition of both photons in the Plastic Ball and in the Inner Shell detectors, as well as the energy and the momentum of ^{10}B using the Heavy Ion detector have been measured. Also, in order to achieve a clean selection of particles, the timing information of all detected particles was recorded during the experiment. The two-photon invariant mass is calculated as follows:

$$M_{\gamma\gamma} = \sqrt{2E_{\gamma high}E_{\gamma low}(1 - cos(\alpha))}, \tag{5.21}$$

where $E_{\gamma high}$ and $E_{\gamma low}$ correspond to the energies of the photon with the higher and the lower energy, respectively, and α is the opening angle of the two photons. Also

$$\begin{aligned} cos(\alpha) = & sin\theta_{\gamma high} * sin\theta_{\gamma low} * cos\phi_{\gamma high} * cos\phi_{\gamma low} \\ & + sin\theta_{\gamma high} * sin\theta_{\gamma low} * sin\phi_{\gamma high} * sin\phi_{\gamma low} \\ & + cos\theta_{\gamma high} * cos\theta_{\gamma low}, \end{aligned}$$

in which $\theta_{\gamma high}(\theta_{\gamma low})$ and $\phi_{\gamma high}(\phi_{\gamma low})$ are polar and azimuthal angles of the photon with the higher (lower) energy. In order to reconstruct the two-photon invariant mass, only two measured observables among $E_{\gamma high}$, $E_{\gamma low}$ and α are needed, since on basis of kinematical constraints the rest of the needed information can be calculated. Three different methods for the invariant mass reconstruction can be applied.

- Method 1: The measured two-photon opening angle, the measured ^{10}B momentum to calculate the π^0 energy, and the measured energy of the photon with the higher energy from the π^0 decay are used. By subtracting the energy of the photon with the higher energy from the pion energy, the energy of the photon with the lower energy produced in the π^0 decay is calculated:

  $$\begin{cases} \alpha: \text{ from the measured angles} \\ E_{\gamma high}: \text{ the measured energy by the Plastic Ball and the Inner Shell detectors} \\ E_{^{10}B}: \text{ the measured energy of } ^{10}\text{B using the Heavy Ion detector} \\ E_{\pi^0} = E_{total} - E_{^{10}B}, \\ E_{\gamma low} = E_{\pi^0} - E_{\gamma high} \end{cases}$$

  where $E_{total} = T_{beam} + M_{^4He} + M_{^6Li}$ is the total available energy. E_{π^0} and T_{beam} are the pion total energy and the kinetic energy of the ^{4}He beam (236.4 MeV), respectively.

- Method 2: The measured two-photon opening angle and the measured ^{10}B momentum are used to calculate the π^0 energy. Using kinematical constraints and the energy of π^0, the energy of the photon with the higher energy is reconstructed. By subtracting the energy of the photon with the higher energy from the pion energy, the energy of the photon with the lower energy is obtained:

  $$\begin{cases} \alpha: \text{ from the measured angles} \\ E_{^{10}B}: \text{ the measured energy of } ^{10}\text{B using the Heavy Ion detector} \\ E_{\pi^0} = E_{total} - E_{^{10}B}. \end{cases}$$

The kinematical constraints are:

$$\begin{cases} \vec{p}_{x\gamma_{high}} + \vec{p}_{x\gamma_{low}} + \vec{p}_{x^{10}B} = 0 \\ \vec{p}_{y\gamma_{high}} + \vec{p}_{y\gamma_{low}} + \vec{p}_{y^{10}B} = 0 \\ \vec{p}_{z\gamma_{high}} + \vec{p}_{z\gamma_{low}} + \vec{p}_{z^{10}B} = \vec{p}_{beam} \\ \mid \vec{p}_{x^{10}B} \mid^2 + \mid \vec{p}_{y^{10}B} \mid^2 + \mid \vec{p}_{z^{10}B} \mid^2 = (E_{total} - E_{\gamma high} - E_{\gamma low})^2 - M^2_{^{10}B}. \end{cases}$$

After simplification of the kinematical conditions, the photon energies are obtained:

$$\begin{cases} E_{\gamma high} = \frac{p^2_{beam} + M^2_{^{10}B} - E^2_{total} - 2E_{\gamma low}(p_{beam} cos\theta_{\gamma low} - E_{total})}{2(p_{beam} cos\theta_{\gamma high} - E_{total}) + 2E_{\gamma low}(1 - cos\alpha)} \\ E_{\gamma low} = E_{\pi^0} - E_{\gamma high}, \end{cases}$$

where $M_{^{10}B}$ is the ^{10}B mass.

- Method 3: The measured two-photon opening angle and the measured energy of the photon with the higher energy are used. In this method, the measured ^{10}B momentum is not used. In order to reconstruct the energy of the photon with the lower energy and the momentum of ^{10}B, kinematical constraints are applied.

$$\begin{cases} \alpha: \text{ from the measured angles,} \\ E_{\gamma high}: \text{ the energy measured by the Plastic Ball and the Inner Shell detectors,} \end{cases}$$

$$\begin{cases} E_{\gamma low} = \frac{p^2_{beam} + M^2_{^{10}B} - E^2_{total} - 2E_{\gamma high}(p_{beam} cos\theta_{\gamma high} - E_{total})}{2(p_{beam} cos\theta_{\gamma low} - E_{total}) + 2E_{\gamma high}(1 - cos\alpha)} \\ E_{\pi^0} = E_{\gamma high} + E_{\gamma low} \\ E_{^{10}B} = E_{total} - E_{\pi^0} \end{cases}$$

In our experimental setup all particles are measured in over-determined kinematics, but with limited resolution. Since the two-photon opening angle, the ^{10}B momentum and the energy of the photon with higher energy deposition were the best constrained observables in our experiment, we decided to use Method 1 for the pion invariant mass reconstruction.

5.4.3 Presort

In the experiment various triggers were used (see Chapter 4). The ^{6}Li(^{4}He,π^0)^{10}B* events represent only a very small subset of the total amount of data which were stored because the main trigger was in many cases generated by other reactions. An example is elastically scattered ^{6}Li particles leading to the Heavy Ion trigger condition, in coincidence with a cosmic ray detected by the Plastic Ball. As can be seen in Fig. 5.1, the raw data are presorted to limit the data set to a reasonable size for further analysis. The presorting algorithm for the ^{6}Li(^{4}He,π^0)^{10}B* event selection reduces the data set by approximately 98.2% by selecting two or more photon tracks in the Plastic Ball. After presorting and final particle selection, which will be explained in Section 5.4.4, the pion track was defined such that at least two separate Plastic Ball clusters in coincidence with ^{10}B should be detected.

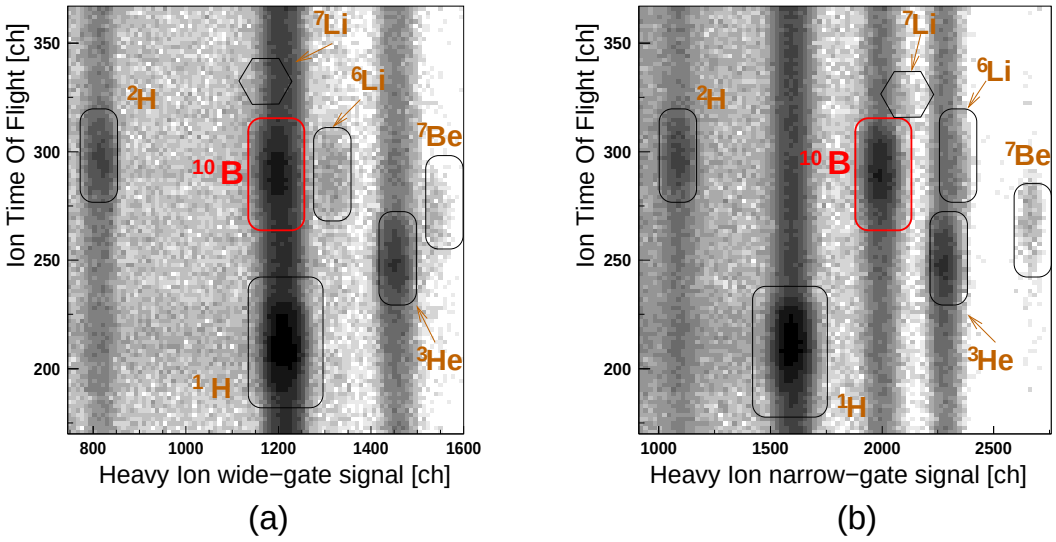

Figure 5.22: (a): The ion Time Of Flight versus the Heavy Ion wide-gate signal. (b): The ion Time Of Flight versus the Heavy Ion narrow-gate signal

5.4.4 Final selections

After presorting the data, final selections to obtain background-free events were applied. In order to select photons and exclude charged particles in the Plastic Ball, only events around the diagonal line in the pulse shape spectrum of the Plastic Ball modules were selected. In the Plastic Ball and the Inner Shell time distribution, only events found in the sharp peaks (regions between two dashed lines) in Fig. 5.2 were selected. In case of the Heavy Ion detector, events which are associated with ^{10}B in the pulse shape spectrum (Fig. 5.4) and the Time Of Flight spectrum (Fig. 5.5) of the Heavy Ion detector have been selected. This selection cut was performed on the 2-dimensional histograms of the Time Of Flight versus the result of the wide-gate integration as well as the Time Of Flight versus the result of the narrow-gate integration (Fig. 5.22).

In addition to the above selections and in order to isolate pionic fusion events which are cleanly separated from the background events, more selections on the momentum distribution of ^{10}B and the opening angle distribution of two photons have been applied and will be discussed in the following sections.

Momentum distribution of ^{10}B

Figure 5.23 shows the Heavy Ion detectors that are hit by ions in the ^{10}B peak which are in coincidence with two photons and therefore are ^{10}B candidates, obtained from Method 1 (a) and Method 2 (b) of the π^0 invariant mass reconstruction. As can be seen, the general behaviour is like a two-peak structure related to the top and bottom rows of the Heavy Ion detector array (see Fig. 5.11 and Fig. 4.5-(i)). Due to the kinematical constraints that are applied in Method 2, peaks in Fig. 5.23-(b) are well separated. In order to exclude background events from the momentum distribution, the same region of the momentum which has been obtained using Method 2, was selected in Method

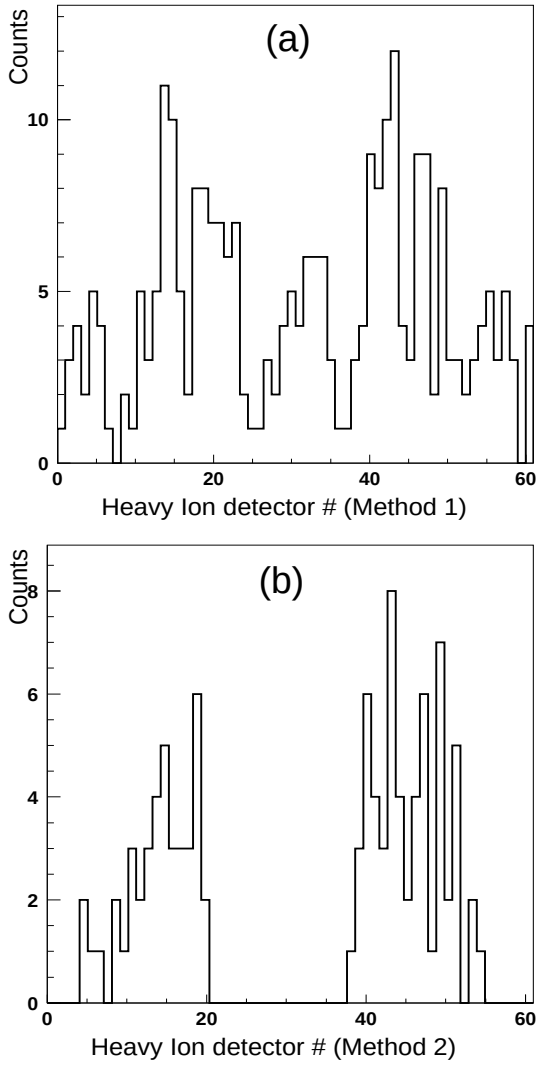

Figure 5.23: The counts measured in the Heavy Ion detector modules hit by ions in coincidence with two photons. Panel (a) shows the result when using the first method of the pion invariant mass reconstruction and the results shown in panel (b) correspond to the second method of the pion invariant mass reconstruction.

1. The selected regions for events in the upper and lower row of the array are shown in Fig. 5.24 as the region between two dashed and two dotted lines, respectively. In Fig. 5.24, events in the two windows represented by the solid line are not associated with ^{10}B. These events are called additional events and correspond to the momentum larger than 1370 MeV/c. The additional events do not produce the two-photon invariant mass with similar distribution that is expected from the phase-space simulation. In fact, events between the two dashed lines or between the two dotted lines but outside the windows in Fig. 5.24 are associated with the two-photon invariant mass distribution which is in a very good agreement with the one from the phase-space simulation (see Section 6.4). In order to find the source of the additional events, various possibilities have been studied. First,

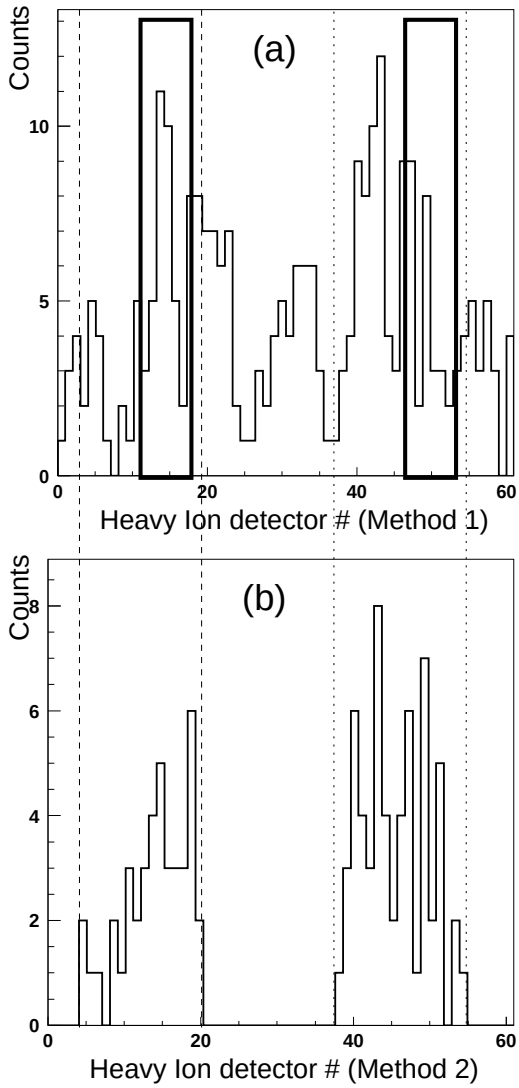

Figure 5.24: The same description as Fig. 5.23. Events in the region between the two dashed (dotted) lines are the accepted events as ^{10}B in the upper (lower) row of the Heavy Ion array by Method 2 of the π^0 invariant mass reconstruction. The two windows represented by the solid line show the events which are originated from the random coincidences. These events are excluded from the further analysis.

it should be noticed that in the pionic fusion reaction of ^{6}Li(^{4}He,π^0)^{10}B* with about 10 MeV available energy above the coherent threshold in the centre-of-mass system, only a few states of ^{10}B, defined by the conservation of isospin (see Fig. 1.5) are allowed to be excited. A Monte-Carlo simulation was performed in order to study the momentum distribution of ^{10}B when it is produced in the excited state. The dashed and dotted curves in Fig. 5.25-(a) show the phase-space simulated ^{10}B momentum distribution when ^{10}B is produced in the state at 1.7402 MeV (J^p, I:0^+,1) and the examined state at 5.1639 MeV (J^p, I:2^+,1). In addition, the solid curve shows the measured ^{10}B momentum distribution

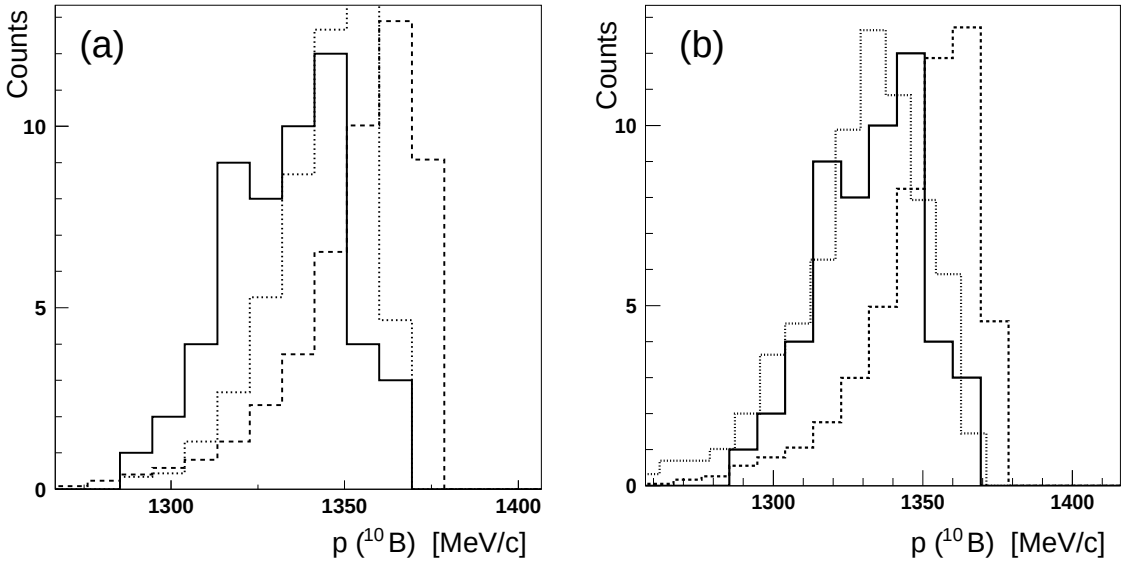

Figure 5.25: (a): The solid curve shows the momentum distribution of ^{10}B resulting from the measured data from the lower row of the Heavy Ion detector array. The dashed curve shows the momentum distribution of ^{10}B from the phase-space simulation of the ^{6}Li(^{4}He,π^0)^{10}B* reaction when ^{10}B is produced in the state at 1.7402 MeV. The dotted curve is the result of the phase-space simulation when ^{10}B is produced in the examined state at 5.1639 MeV. The simulated results were obtained using the pure ^{6}Li target. (b): The dotted curve is the phase-space simulation of the ^{10}B momentum distribution when the target is not pure ^{6}Li but has about 17%±3% ^{16}O as contamination. The data cover the same region as the phase-space simulation using the pure ^{6}Li target, but are in better agreement with the simulation when 17% ^{16}O as target contamination is used in the phase-space simulation.

obtained from the lower row of the Heavy Ion array, when events with momentum larger than 1370 MeV/c are excluded. As can be seen, the simulated momentum distribution of ^{10}B produced in the examined state at 5.1639 MeV covers the same region as the result for producing the 1.7402 MeV state and the experimental result when events with momentum larger than 1370 MeV/c are excluded. Therefore, the additional events do not correspond to the produced ^{10}B in the higher excited states. Furthermore, ^{10}B particles originating from ^{16}O(^{4}He,π^0)^{10}B+X reaction (pionic fusion of ^{4}He with the existing ^{16}O in the ^{6}Li target) are not accepted by the BBS window (see Section 5.5) and therefore can not explain the additional events. Additional events are not associated with ^{4}He particles originating from the elastic interaction of ^{4}He and ^{6}Li due to the fact that the acceptance of the BBS window suppresses the ^{4}He particles. The coincidence of the neighbouring Heavy Ion detector modules corresponding to both regions of the momentum ($p_{^{10}B} \leq$1370 MeV/c and $p_{^{10}B} >$1370 MeV/c) has been checked in order to see if the additional events are the result of an incomplete energy deposition inside the relevant detectors. No coincidence between the detector groups in two regions of the momentum was found (see the next chapter). Since the simulated results do not show that those events are ^{10}B, the conclusion was that the additional events are random coincidences. Those additional events were not

included in the further analysis. The azimuthal asymmetry in the number of accepted ^{10}B events can be explained by the asymmetric acceptance of the Plastic Ball due to target equipments (see Fig 4.6) in the following way. Missing modules in the forward region near ϕ=90° will cause a reduced number of two-photon coincidences with the backward photon near -90°. These photons are correlated with ^{10}B moving preferentially to the upper part of the Heavy Ion detector array.

In Fig. 5.25-(b) the solid curve shows the measured ^{10}B momentum distribution using the lower part of the Heavy Ion detector array and the dashed curve corresponds to the result of the phase-space simulation. The measured momentum distribution covers the same region as the result of the phase-space simulation but the peak is shifted to the lower momentum region by less than 2%. As was mentioned in Section 4.3, to prevent oxidation, the ^{6}Li target was kept in an argon atmosphere during the preparation process and the transport to the vacuum chamber. However, by comparing the simulated results of the reaction with the pure and the oxidised ^{6}Li target in the phase-space simulation, it was found that about 17±3% of the target nuclei were ^{16}O. Using this combination for the target in the simulation, the simulated momentum distribution is shifted to lower momentum in the same way as the result of the experimental data (Fig. 5.25-(b) dotted curve).

Opening angle distribution of two photons

The opening angle of two photons is calculated as follows:

$$\begin{aligned}\theta_{\gamma\gamma} = acos(&sin\theta_{\gamma high} * sin\theta_{\gamma low} * cos\phi_{\gamma high} * cos\phi_{\gamma low} \\ &+ sin\theta_{\gamma high} * sin\theta_{\gamma low} * sin\phi_{\gamma high} * sin\phi_{\gamma low} \\ &+ cos\theta_{\gamma high} * cos\theta_{\gamma low}).\end{aligned}$$

In Fig. 5.26, the solid curve shows the opening angle distribution of two separated clusters as the positions of two photons in the present data. Since in our experiment the available energy above the coherent threshold of the ^{6}Li(^{4}He,π^0)^{10}B* reaction was 10 MeV, the produced pions have small kinetic energy (<9.4 MeV). Therefore, due to the kinematical constraints, the two photons are produced with a large opening angle.

The dashed curve in Fig. 5.26 shows the opening angle distribution of the two photons obtained from the Monte-Carlo simulation. There appear two peak structures. The peak in the lower region of the opening angle distribution is the result of producing "split-offs" after clustering of the Plastic Ball. As was mentioned in Section 5.4.1, after improving the clustering of the Plastic Ball, the number of split-offs was reduced to less than 3%, however, the number of different combinations made by the split-offs (either split-offs with split-offs or split-offs with the main clusters) for the pair of clusters is about 20% of the total number of combinations. Therefore, there is still a visible increase of the yield in the region of small opening angles. The second peak shown by the dashed curve is mainly related to the combination of the main clusters and is located around 150°.

The simulated distribution shown by the dashed curve has different peak position and width compared to the measured distribution. This can be caused by the limited position resolution in the Plastic Ball scintillators for low energy deposition which has not yet been taken into account in the simulation. We call the simulated and observed resolutions

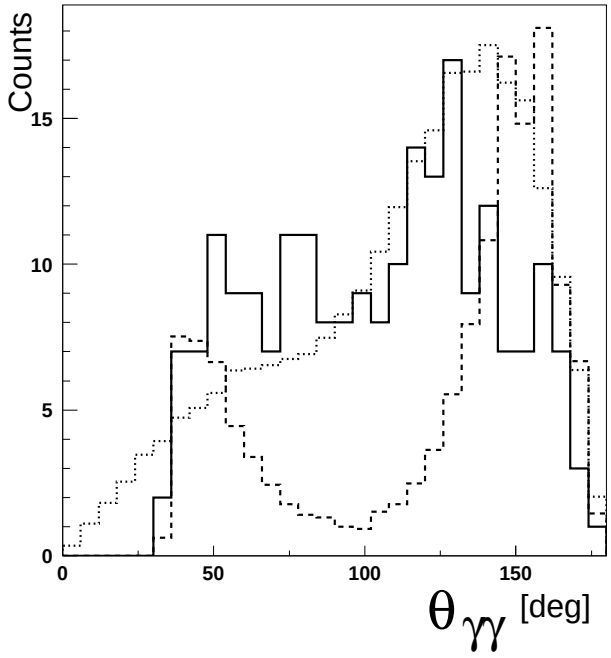

Figure 5.26: The solid line shows the opening angle distribution of two photons in the data. The dashed and dotted curves are the opening angle distribution from the Monte-Carlo simulation using the ideal and the real resolution of the angle determination for the Plastic Ball, respectively. The simulated results are down scaled. For all the results, the improved clustering method for the Plastic Ball has been used.

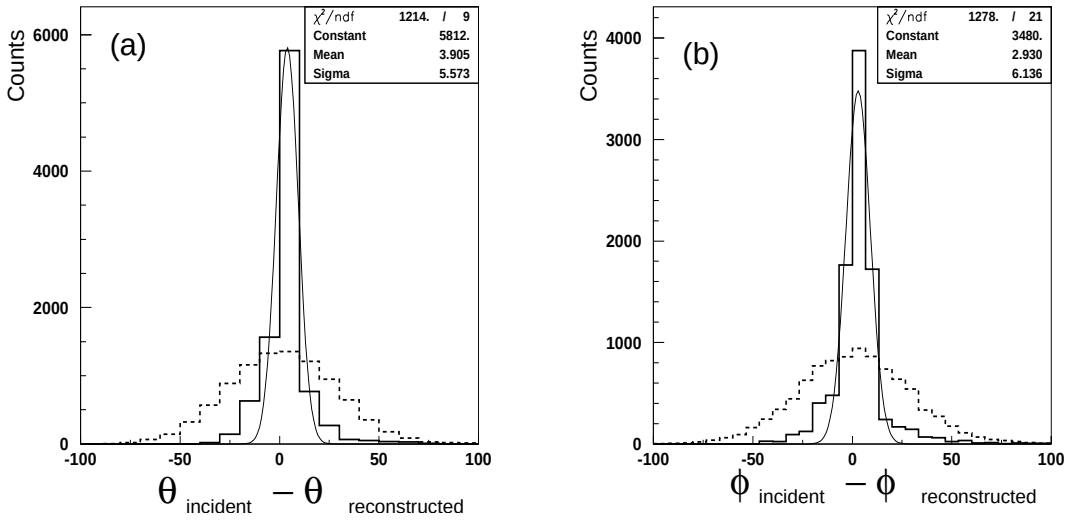

Figure 5.27: Panel (a) shows the difference of the incident and the reconstructed polar angles and panel (b) indicates the difference of the incident and the reconstructed azimuthal angles for a single photon produced in the Monte-Carlo simulation. The solid and dashed curves are the results when using the ideal and the real resolutions of the angle determination, respectively.

of the angle determination the "ideal resolution" and "real resolution", respectively. It should be noted that Fig. 5.21 shows the ideal resolution. To determine and apply the real resolution in the simulation, single photons with E_γ=69 MeV were analysed in the Monte-Carlo simulation. The ideal resolutions of the angle determination for the polar and azimuthal angles of the single photons are 5.6° and 6.1° (σ), respectively (Fig. 5.27-solid curve). Two different factors for the photon polar and azimuthal angles (which were reconstructed according to the Plastic Ball module angles) were calculated by the same method that was explained in Section 5.3.2, to match the angular resolution of the detectors for the simulated photons. After applying those factors (the smearing effects), resolutions of the angle determination for the polar and azimuthal angles were changed to 26.8° and 27.2° (σ), respectively. Figure 5.27 shows the simulated difference of the incident and the reconstructed polar (a) and azimuthal (b) angles for single photons. The solid and dashed curves are the results considering the ideal and the real resolution of the angle determination, respectively. Using the real resolutions of the angle determination in the simulation, the measured distribution of the opening angle are reproduced (Fig. 5.26-dotted curve). For further analysis, only the pairs of clusters with opening angle larger than 94° have been selected.

5.4.5 Energy reconstruction of two decay photons

For the reconstruction of the pion invariant mass the measured photon energies are used. In this section, we verify that the reconstructed energy distribution can be understood on basis of phase-space Monte-Carlo simulations. According to the Monte-Carlo simulations, photons from the π^0 decay moving in the backward direction of the setup deposit part of their energy in the Inner Shell modules. However, due to the low efficiency of the Plastic Ball for photon detection (see Section 5.6), backward photons do not deposit all the rest of their energy into the Plastic Ball. Furthermore, in case of the forward photons, the energy deposition is only a fraction of their original energy. In order to reconstruct the original photon energies from the deposited energy, a Monte-Carlo simulation of the ^{6}Li(^{4}He,π^0)^{10}B* reaction has been performed. The same normalisation factor which was obtained from the simulation was used to reconstruct the measured photon energies. The reconstructed energy of the photon with the higher deposition in the Plastic Ball module cluster or in the Inner Shell module plus the Plastic Ball module cluster behind is shown in Fig. 5.28. The solid and dashed curves show the result of the data and the simulation, respectively, summed over all the modules. The simulated yield is downscaled. There is a good agreement in the peak position, shape of the distribution and the covered region of the distribution between the measured and the simulated results.

5.5 Data contamination and background events

As was explained in Section 5.4.4, during the experiment the ^{6}Li target was contaminated by about 17%±3% Oxygen due to oxidation. Therefore one source of contamination can be the interaction of ^{4}He with ^{16}O. Using the Monte-Carlo simulation, the reaction of ^{16}O(^{4}He,π^0)^{10}B+X was studied. "X" denotes the third particle that must be produced in this reaction. Figure 5.29 shows the momentum distribution of the produced ^{10}B without taking the acceptance of the Big-Bite Spectrometer into account. The solid

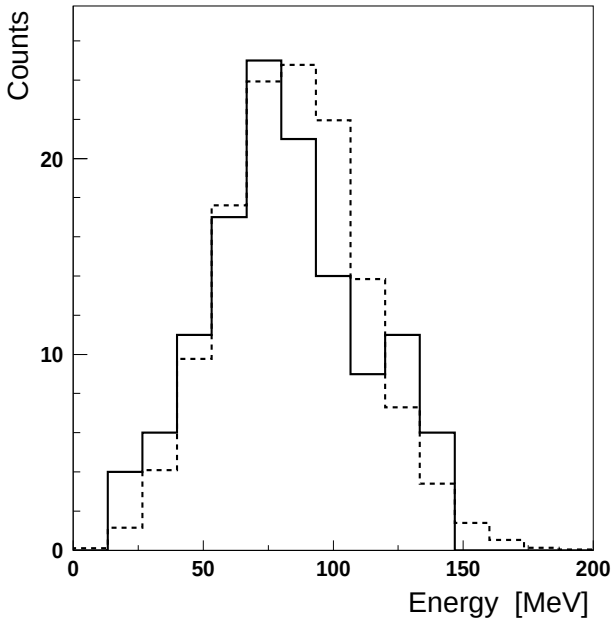

Figure 5.28: The reconstructed energy spectrum of photons with the higher energy deposition in the Plastic Ball module cluster or in the Inner Shell module plus the Plastic Ball module cluster behind. The solid and dashed curves are the measured and the simulated results, respectively.

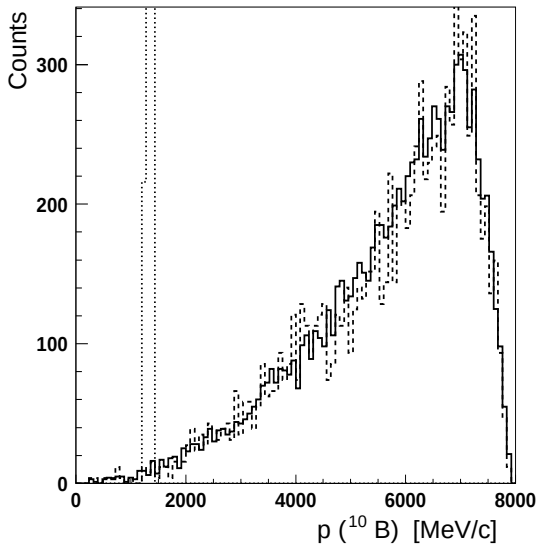

Figure 5.29: The momentum distribution of the produced ^{10}B. The solid and dashed curves represent the momentum distribution of ^{10}B resulting from the ^{16}O(^{4}He,π^{0})^{10}B+X reaction when 20% and 10% of the target are ^{16}O, respectively. The histogram indicated by the solid curve is down scaled by a factor 2. The dotted curve is the result of the ^{6}Li(^{4}He,π^{0})^{10}B* reaction on a pure ^{6}Li target

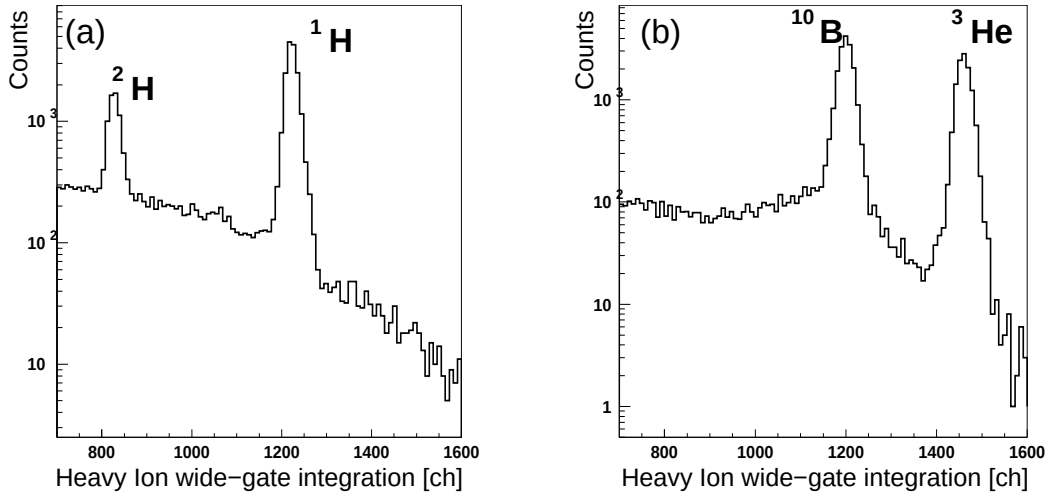

Figure 5.30: Evaluation of the peak to background ratio. (a): The projection of the line including ^{2}H and ^{1}H peaks in the Heavy Ion pulse shape spectrum (Fig. 5.4) on the x-axis. (b): The projection of the line including ^{10}B and ^{3}He peaks in the Heavy Ion pulse shape spectrum on the x-axis.

and dashed curves are presenting the momentum distribution of ^{10}B resulting from the ^{16}O(^{4}He,π^{0})^{10}B+X reaction when 20% and 10% of the target is ^{16}O, respectively. In this study, the nominal thickness of the target is the same as the used ^{6}Li target during the experiment (2 mg/cm^{2}). The dotted line is the result of the ^{6}Li(^{4}He,π^{0})^{10}B* reaction on a pure ^{6}Li target. By applying the acceptance of the Big-Bite Spectrometer, it is shown that independent of the ^{16}O percentage in the target, only less than 0.12% of the produced ^{10}B from the ^{16}O(^{4}He,π^{0})^{10}B+X reaction can enter the BBS window, but the acceptance of the Heavy Ion detector for those events is very small and negligible. Therefore the corresponding events were not registered during the experiment.

A large fraction of the data includes other reaction channels. Using the Heavy Ion detector, in addition to ^{10}B some particles from the other reaction channels have been measured. Different peaks in the Heavy Ion pulse shape spectrum (Fig. 5.4) represent different particles. The width of every peak is related to the detector response, kinematical broadening and straggling in the target. Events outside the main peaks are related to random coincidences between Plastic Ball and Heavy Ion detectors and can be rejected by suitable windows on the ion Time Of Flight as shown in Fig. 5.22. Figure 5.30-(a) shows the projection of the line including ^{2}H and ^{1}H peaks in the Heavy Ion pulse shape spectrum on the x-axis. Figure 5.30-(b) displays the projection of the line including ^{10}B and ^{3}He. In the Heavy Ion pulse shape spectrum (Fig. 5.4), the minimum ratio of the peak to background is about 4 and this occurs for the lowest deposited energies. With increasing energy, this ratio will increase to more than 20. In case of the ^{10}B peak, the peak to background ratio is higher than 50, which makes the selection rather clean.

5.6 Acceptance corrections

Due to the systematic limitations of the experimental setup, not all the produced events can be detected. The acceptance provides us an account of events that will not be detected either due to the limited phase-space coverage of the apparatus, that is e.g. if the detector is not placed or functioning properly (geometrical acceptance) or due to the inefficiency. The efficiency of the measurement gives us an estimate how often a reaction will be registered with our experimental apparatus, that is e.g. when an event is registered in one part of the setup (like the Inner Shell) and not in the other part (like the Plastic Ball) or when a particle is not detected because of some detection threshold. In order to obtain reliable cross section results, correction factors for the acceptance have to be applied. The event generator GENBOD [52] was applied to produce kinematically allowed events and study the acceptance of the detectors for the reaction of ^{6}Li(^{4}He,π^{0})^{10}B*. The details of the detector setup were simulated by the detector-simulation program GEANT3 [53]. As was mentioned in Section 3.5, by combining the event generator and the detector-simulation program, simulated data were obtained and analysed with similar cuts and thresholds as experimental data.

The Big-Bite Spectrometer and the Heavy Ion detector

Figure 3.3-(a) shows the scatter plot of the simulated vertical and horizontal angle of incidence of ^{10}B in the Big-Bite Spectrometer. The vertical and the horizontal angles are defined as the projection of the angle in the y-z plane and the x-z plane, respectively, where the positive z-direction is the beam direction. The dashed line is the window of the BBS entrance. The vertical and the horizontal acceptances of the Big-Bite Spectrometer for ^{10}B, defined as the ratio of the accepted ^{10}B particles at the BBS window over the number of produced ^{10}B particles, are 100% and 86%, respectively.

To relate the measured quantities in the Heavy Ion detector to parameters of the reactions at the target, one has to transport the particles through the spectrometer and this procedure is called ray-tracing. To connect the parameters at the target, referred as the subscript "t", and at the Heavy Ion detector, subscripted by "h", one uses a transfer matrix whose elements are the coefficients of the Taylor expansion to describe deviations from the central reference trajectory

$$\alpha_t = \sum_{\mu,\nu,\lambda,\eta} (\alpha \mid x^{\mu}\theta^{\nu}y^{\lambda}\phi^{\eta})\; x_h^{\mu}\theta_h^{\nu}y_h^{\lambda}\phi_h^{\eta}. \tag{5.22}$$

The target variables are denoted by α and can be θ, ϕ or δ. The coordinates x and θ are the distance and angle in the horizontal direction and similarly y and ϕ for the vertical direction. δ is the deviation of the rigidity Bρ of the particle with respect to a particle travelling along the central ray of the spectrometer. The ray-tracing method was used to trace ^{10}B inside the Big-Bite Spectrometer and to calculate the Heavy Ion acceptance (see Fig. 5.11). As origin of ^{10}B in the target a point slightly off centre was chosen, displaced by x_0 horizontally and y_0 vertically. This takes care of the finite size of the beam spot on the target. Figure 5.31 shows the position of ^{10}B in the Heavy Ion detector for different energies and different vertical angles ϕ= -4.02°, -1.9°, 0°, 1.9° and 4.02° at the entrance of the Big-Bite Spectrometer. Figure 5.31-(a) shows the results when ^{10}B originates from a

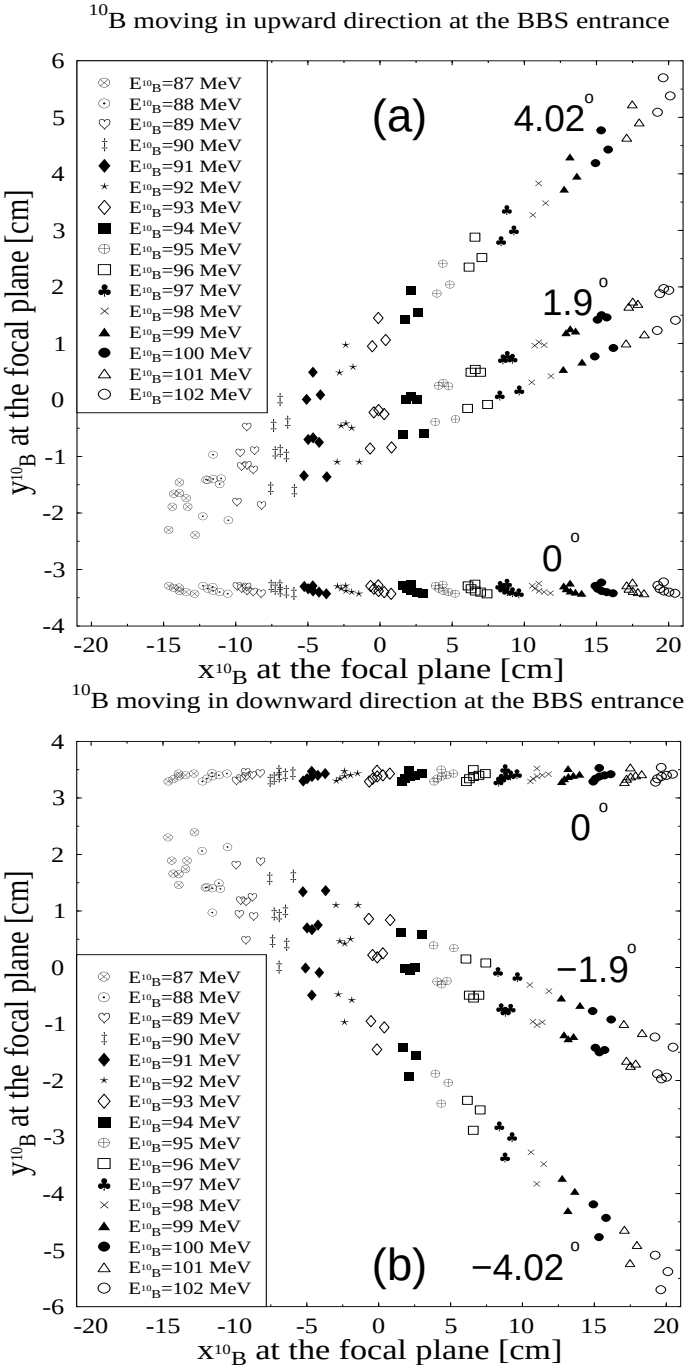

Figure 5.31: (a) ((b)): The position of a ^{10}B ion at the Heavy Ion detector if ^{10}B originates from a position in the target at x_0=0.1 cm and y_0=0.5 cm (y_0=-0.5 cm) and moves in the upward (downward) direction when entering the Big-Bite Spectrometer. Different symbols show different energies of ^{10}B and different points with the same symbol are representing different chosen rays for tracing. The vertical and horizontal axes correspond to the vertical and horizontal positions of ^{10}B ions with respect to the beam direction. Numbers 4.02°, 1.9° and 0° (-4.02°, -1.9° and 0°) are the vertical angles of ^{10}B at the BBS entrance.

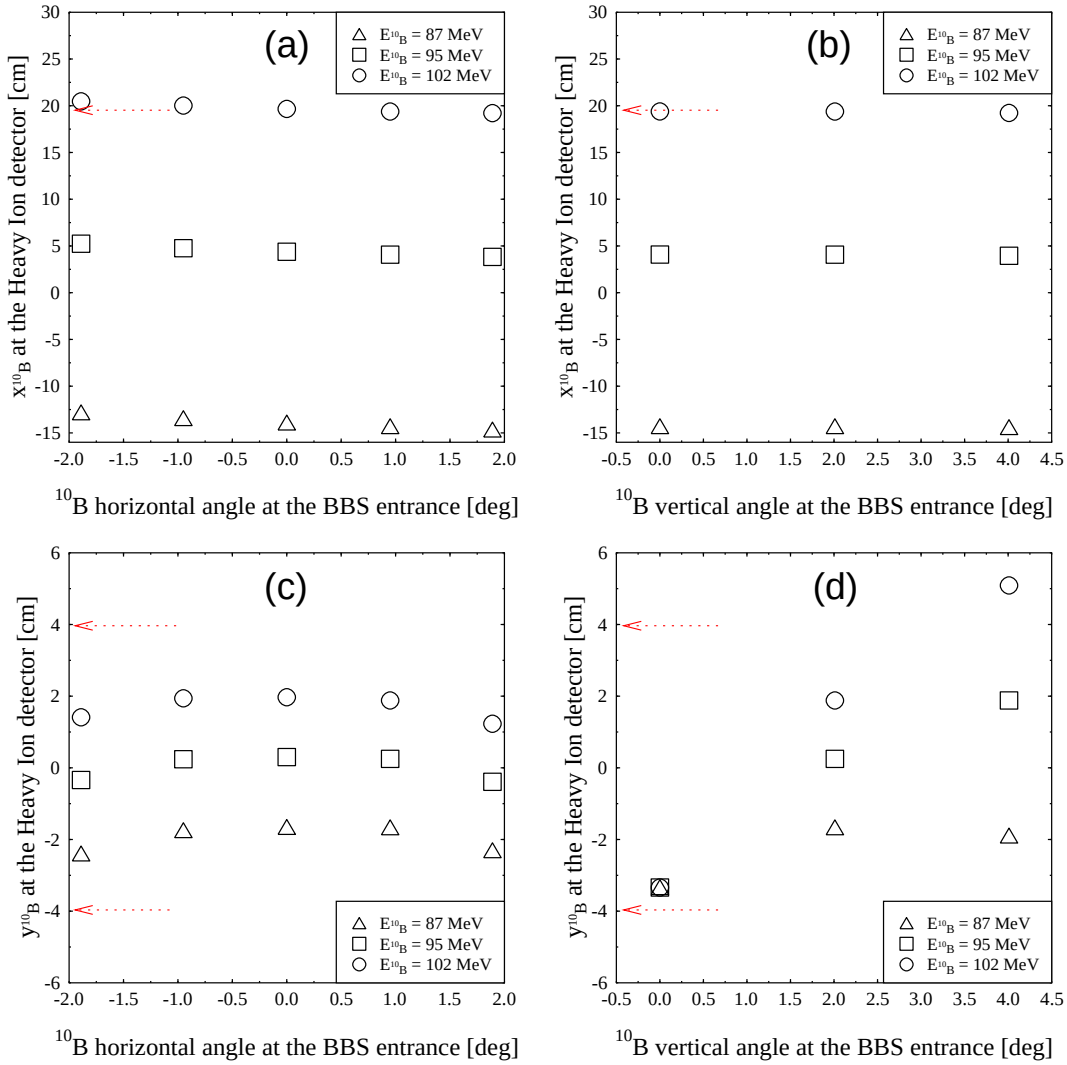

Figure 5.32: (a): The ^{10}B horizontal position in the Heavy Ion detector array as a function of the ^{10}B horizontal angle at the BBS entrance. In this plot, the ^{10}B vertical angle at the BBS entrance is 2.01°. (b): The ^{10}B horizontal position in the Heavy Ion detector array as a function of the ^{10}B positive vertical angle at the BBS entrance. The ^{10}B horizontal angle at the BBS entrance is 0.95°. (c): The ^{10}B vertical position in the Heavy Ion detector array as a function of the ^{10}B horizontal angle at the BBS entrance. The ^{10}B vertical angle at the BBS entrance is 2.01°. (d): The ^{10}B vertical position in the Heavy Ion detector array as a function of the ^{10}B positive vertical angle at the BBS entrance. The ^{10}B horizontal angle at the BBS entrance is 0.95°. The original position of ^{10}B in the target has been chosen at x_0=0.1 cm and y_0=0.5 cm.

position in the target at x_0=0.1 cm and y_0=0.5 cm, while shown in panel (b) are the results when x_0=0.1 cm and y_0=-0.5 cm. In case ϕ=0° and ϕ=±1.9°, the results associated with θ=0°, θ=±0.95° and θ=±1.89° are presented. In case ϕ=±4.02°, the results associated with θ=0° and θ=±0.95° are shown. Only ^{10}B ions with energies larger than 99 MeV and the vertical angle $\phi \geq$4.02° (70 mrad) or $\phi \leq$-4.02° at the BBS entrance can go out of

the region where the Heavy Ion detector is located. Since according to the kinematical constraints it is not possible for the produced ^{10}B to have a vertical angle larger than 2.2° at the BBS entrance (Fig. 3.3-(a)), all the produced ^{10}B particles that enter the Big-Bite Spectrometer can be detected by the Heavy Ion detector. Therefore the acceptance of the Heavy Ion detector array for the ^{10}B detection is 100%.

Figure 5.32 represents the location of ^{10}B particles in the Heavy Ion detector array when they have different horizontal and positive vertical angles at the BBS entrance. Different symbols correspond to different energies of ^{10}B at the BBS entrance. Arrows represent the boundaries of the Heavy Ion array. The lower horizontal boundary of the array (-19.5 cm) is not in the range of the upper plots. For a constant ^{10}B energy and by changing the horizontal angle of ^{10}B at the BBS entrance from the minimum (-1.9°) to the maximum (1.9°) horizontal acceptance of the BBS window, the horizontal position of ^{10}B ions in the Heavy Ion detector array will shift by almost 1.85 cm which is equivalent to 1.4 detector units of the Heavy Ion detector (Fig. 5.32-(a)). For a constant ^{10}B energy and a constant horizontal angle of ^{10}B at the BBS entrance, the horizontal position of ^{10}B ions in the Heavy Ion detector array is not dependent on the vertical angle at the BBS entrance (Fig. 5.32-(b)). This observation implies that the BBS resolution for the momentum determination is good.

For a constant ^{10}B energy at the BBS entrance, the vertical position of ^{10}B particles depends on the horizontal and the vertical angles at the BBS entrance (Fig. 5.32-(c) and -(d), respectively). As can be noticed from Fig. 5.32-(c), by changing the horizontal angle of ^{10}B at the BBS entrance, ^{10}B ions do not move out of the vertical boundaries of the Heavy Ion array. In addition, for $E_{^{10}B}$ $\leq$90 MeV, ^{10}B particles with positive (negative) vertical angles in the BBS entrance hit the lower (higher) part of the Heavy Ion detector. If $E_{^{10}B}$ >90 MeV, ^{10}B can be detected either in the lower or in the higher part of the Heavy Ion detector array (Fig. 5.32-(d)). Therefore, it was difficult to use only the vertical position of ^{10}B in the array in order to reconstruct the vertical ^{10}B angle in the BBS entrance. It should be mentioned, however, that for the analysis other measured observables together with the kinematical constraints were sufficient to reconstruct the ^{10}B angular distribution at the BBS entrance.

The Plastic Ball and its Inner Shell

The total acceptances of the Plastic Ball and the Inner Shell for the detection of at least one photon originating from π^0 decay are 44.1% and 56.2%, respectively, mainly due to the geometrical acceptances of the Plastic Ball and the Inner Shell.

By applying similar cuts and thresholds as used for the experimental data, the total acceptance of the Plastic Ball or the Plastic Ball plus Inner Shell for the pion detection including the reconstruction efficiency was obtained as follows:

$$acceptance = \frac{number\ of\ successfully\ reconstructed\ events,\ per\ bin\ (all\ cuts\ included)}{all\ thrown\ events,\ per\ bin} \tag{5.23}$$

In addition, a reconstruction efficiency of 57% was obtained as follows:

$$\frac{number\ of\ successfully\ reconstructed\ events,\ per\ bin\ (all\ cuts\ included)}{all\ accepted\ events\ by\ the\ geometry,\ per\ bin} \tag{5.24}$$

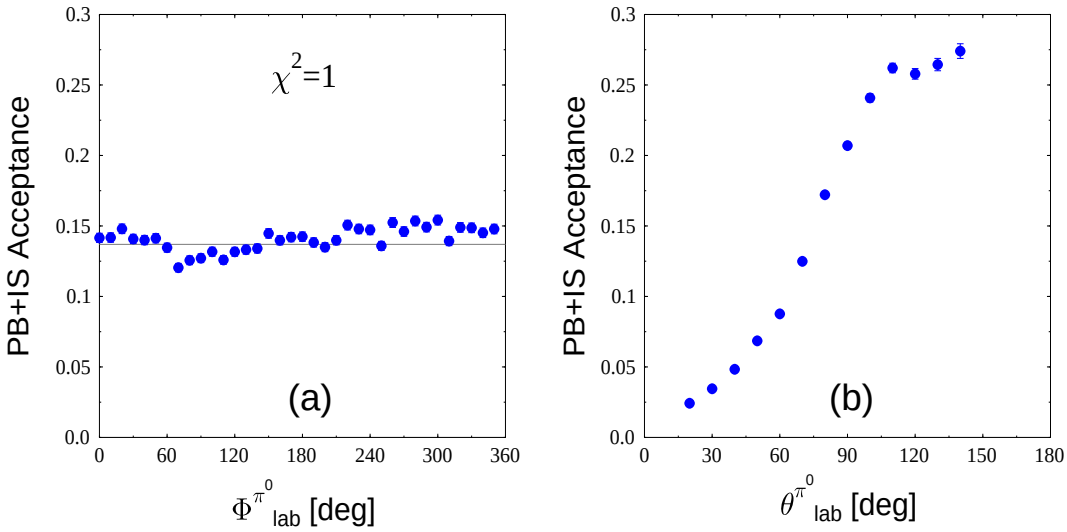

Figure 5.33: PB+IS acceptance for the pion detection.

The overall acceptance of the Plastic Ball together with its Inner Shell for the π^0 detection was calculated and is 14.1%. In Fig. 5.33-(a) and -(b), the acceptance of the Plastic Ball together with its Inner Shell as function of $\Phi^{\pi^0}{}_{lab}$ and $\theta^{\pi^0}{}_{lab}$ (the pion azimuthal and polar angles, in the laboratory system), respectively, is depicted. $\Phi^{\pi^0}{}_{lab}$ has almost a flat acceptance which varies between 12% and 15%. The fitted line to the $\Phi^{\pi^0}{}_{lab}$ acceptance has a reduced χ^2=1. The fluctuations correspond to the geometrical acceptance of the Plastic Ball detector. In our analysis, only two photons that both hit the Plastic Ball modules were selected. Due to the existence of the target equipments at around $\Phi^{\pi^0}{}_{lab}$=90°, there is no Plastic Ball module in that region. Therefore, photons that move to that direction are not selected for the analysis, even though they deposit energy in the Inner Shell module which is in their track. As result, a drop of acceptance can be seen in Fig. 5.33-(a) in the region $0° < \Phi^{\pi^0}{}_{lab} < 180°$, where the upper hemisphere of the Plastic Ball is located (Fig. 4.6). For $\theta^{\pi^0}{}_{lab}$ we see a large variation in acceptance. Variations, especially the drop in acceptance for forward angles ($\theta^{\pi^0}{}_{lab} < 90°$), are caused by solid angle effects due to the fact that the Plastic Ball coverage limits the acceptance for the photon polar angles $50° < \theta^{\gamma}{}_{lab} < 160°$. Another reason for the drop in the acceptance for the most forward angles is the escape of the electromagnetic showers from the edges of the scintillators of the Plastic Ball and the Inner Shell. In addition, due to the existence of the Inner Shell, the efficiency of photon detection in the backward part of the geometry is higher than in the forward part.

5.7 Data normalisation and the experimental cross section

The differential cross section has been determined as a function of $\theta^{\pi^0}_{cm}$. In order to obtain the absolute scale of the distribution, the number of produced pions must be normalised. In the normalisation procedure, experimental parameters like the target thickness, the number of incident ^{4}He particles and the acceptance of the experimental setup were taken

into account. The number of incident particles in the beam was calculated using the total charge collected by the Faraday Cup. In addition, the bin size of the measured values for the angles has been entered into the normalisation. The differential cross section was calculated as follows:

$$\frac{d\sigma}{d\Omega} = \frac{N_{\pi^0}}{N_i \times N_t \times LT \times a_{PB+IS} \times a_{BBS} \times a_{HI} \times \epsilon_{rec} \times \Delta\Omega}, \tag{5.25}$$

where

- N_{π^0} : number of detected neutral pions in every angle bin,
- N_i : total number of ^{4}He particle projectiles,
- N_t : number of ^{6}Li particles per cm^2 in the target,
- LT : electronic live-time,
- a_{PB+IS} : acceptance of the Plastic Ball and the Inner Shell (backward acceptance) or the Plastic Ball only per angle (forward acceptance) for the pion detection: $\frac{N^{out}_{\pi^0}}{N^{in}_{\pi^0}}$,
- a_{BBS} : acceptance of the BBS for the ^{10}B detection,
- a_{HI} : acceptance of the Heavy Ion detector array for the ^{10}B detection,
- ϵ_{rec} : efficiency of the pion reconstruction,
- $\Delta\Omega$: bin size of the solid angle for a Plastic Ball module at a particular scattering angle.

The number of incoming ^{4}He particles was calculated from the measurement of the total integrated charge in the Faraday Cup (FC). The relative accuracy of this method was estimated to be 8%. The measurement of the integrated charge was corrected for the dead-time of the data acquisition electronics (49%) resulting in $1.9{\cdot}10^6$ nC which is equivalent to N_i =$6.05{\cdot}10^{15}$. Using the nominal thickness of the ^{6}Li target (2 mg/cm^2), N_t was calculated as $1.74{\cdot}10^{20}$ cm^{-2}. In general a differential cross section is reported in b/sr. N_{π^0} in our experiment is 101. By normalisation, the experimentally measured cross section integrated over the whole acceptance of the detector setup can be obtained and is reported in the next chapter. A summary of all applied corrections to calculate the cross section is listed in Table 5.3.

Table 5.3: Summary of all applied corrections for detector acceptances and efficiencies together with the measured values which have been used to calculate the cross section.

Plastic Ball acceptance for detection of at least one photon from π^0 decay	44.1%	Inner Shell acceptance for detection of at least one photon from π^0 decay	56.2
BBS acceptance for the ^{10}B detection	86%	Heavy Ion detector acceptance for the ^{10}B detection	100%
PB+IS acceptance for the π^0 detection	14.1%	BBS+HI detector acceptance for the ^{10}B detection	86%
Reconstruction efficiency	57%	Electronics dead-time	49%
Total number of ^{4}He in the beam corrected for the dead-time	6.05 $\cdot 10^{15}$	Total accumulated charge by the Faraday Cup corrected for the dead-time	1.9 $\cdot 10^{6}$ nC
Number of ^{6}Li particles per cm^2 in the target	1.74 $\cdot 10^{20}$	Nominal target thickness	2 mg/cm^2
Bin size of the polar angle	10°	Total number of measured π^0	101